DNS for Flow Separation Control around Airfoil by Steady and Pulsed Jets

Shutian Deng[1], Li Jiang[2], and Chaoqun Liu[3]
Department of Mathematics
University of Texas at Arlington, Arlington, TX 76016, USA

cliu@uta.edu

ABSTRACT

This work consists of two parts. The first part is direct numerical simulation (DNS) for flow separation and transition around a NACA 0012 airfoil with an attack angle of 4^0 and Reynolds number of 100,000. The details of the flow separation, formation of the detached shear layer, Kelvin- Helmoholtz instability (inviscid shear layer instability) and vortex shedding, interaction of non-linear waves, breakdown, and re-attachment are obtained and analyzed. Though no external disturbances are introduced in the baseline case study, the self-excited mechanism is observed, which may reveal the origin of the disturbance for airfoil with attack angle. The power spectral density of pressure shows the low frequency of vortex shedding caused by the Kelvin-Helmoholt instability still dominates from the leading edge to trailing edge. The simulation shows that the nonlinear wave interaction and breakdown is driven by the generation and growth of the stream-wise vortex which leads to the deformation, stretching, and eventually breakdown of the shedding prime vortex. The second part is DNS for flow separation control by blowing jets (steady, pulsed, and pitched and screwed jets). The effects of unsteady blowing on the surface at the location just before the separation points on the transition and separation are also studied. The separation zone is significantly reduced (almost removed) after unsteady blowing technology is applied. In this work, DNSUTA, a code with high-order accuracy and high-resolution developed by the CFD group at University of Texas at Arlington CFD is applied

1.0 INTRODUCTION

Flow transition in separation bubbles is a classic topic and has been studied for many years (Boiko et al, 2002). However, most of work were focused on flow around a hump placed on a flat plate (Musad et al, 1994) or for a blunt leading edge (Yang & Voke, 2001). Flow separation and transition around an airfoil with attacked angle is rarely found in literature due to its complexity. The linear stability theory (LST; see Drazin & Reid, 1981) is mainly a local analysis with an assumption of parallel base flow. The parabolized stability equations (PSE; see Bertolotti, 1992) assumes a steady base flow with no elliptic part. These assumptions do not apply for the case of flow separation and transition around airfoil with attack angle where no steady base flow exists and the transition process is dominated by an elliptic process especially in the late stages. Though it is true that the LST and PSE cannot provide a correct prediction for the case, the Kelvin-Helmoholtz instability mechanism in a separated shear layer still dominates the process especially in the early transition stage.

[1] PhD Student
[2] Research Associate
[3] Professor and AIAA Associate Fellow

Paper presented at the RTO AVT Specialists' Meeting on "Enhancement of NATO Military Flight Vehicle Performance by Management of Interacting Boundary Layer Transition and Separation", held in Prague, Czech Republic, 4-7 October 2004, and published in RTO-MP-AVT-111.

Boundary layer separation and transition exist in many engineering flows around wings and blades. When an adverse pressure on a laminar boundary layer over a surface is strong enough, the laminar boundary layer separates from the surface. Separation and transition in these types of flows are strongly coupled. The instability at the separation zone is widely accepted as dedicated by the Kelvin-Helmholtz mechanism. Transition takes place owing to nonlinear breakdown of spatially growing traveling waves in the separated free shear layer (Yang & Voke, 2001). When the shear layer becomes turbulent, the detached shear layer may reattach to the surface, creating a separation bubble and forming attached turbulent boundary layer. Obviously, the length of the bubble is closely related to when and where the transition takes place. On the other hand, the size of the separation bubble could directly affect the flight characteristics of the airfoil and the efficiency of the turbine machine. Understanding of the separation and transition mechanism is of great importance in improvement of design for the aircraft and turbo-machinery.

The flow separation over a wing in flight will cause loss of the lift and increase of the drag which threatens the stability and efficiency of the aircraft. Great efforts have been taken into developing and studying efficient separation control techniques. It has been observed that relatively large quantities of steady blowing near the point of separation can reattach the flow and increase the lift, but the steady blowing may also cause a thickening of both the boundary layer and the wake behind the airfoil which leads to increased drag (Nagib et al, 2001). Experiments conducted by Bons et al (Bons et al, 2001) have shown that the steady Vortex Generator Jets (VGJ) have the effect of reducing or entirely eliminating the separation zone on the suction surface of the blade at low Reynolds number, while the pulsed VGJs produce a comparable improvement to that for steady VGJs but with an order of magnitude less required mass-flow. In contrast to steady blowing, the oscillatory blowing takes advantage of inherent local instabilities in the near-wall shear layer that causes the selective amplification of the input oscillation frequency. These amplified disturbances propagate downstream along the airfoil as coherent large structures that serve to mix the boundary layer flow and delay separation (Negib et al, 2001). It has been concluded by Bons et al (2001) that the beginning and end of the jet pulse provide influences to the boundary layer through the mechanisms of the early boundary layer transition and vortical entrainment of the free-stream fluid. The distance from the jet injection location to the natural separation point is a critical factor in determining the effectiveness of the pulsed blowing. It has also been mentioned that the pitch and screw angles of the jet have significant effects on the vortex structure and effectiveness of the flow separation control.

A fully clarification of this separation control mechanism by triggering early transition is highly desirable. With the advances of the computer resources and numerical methods, high resolution and high accuracy numerical simulation has been becoming feasible and affordable on this type of the DNS study. In this work, high-accuracy and high-resolution numerical simulations are conducted to investigate the details of the separation and transition processes on a NACA 0012 airfoil with or without jet blowing on the suction surface. The effects of different types of blowing on the separation and transition process are investigated. The organization of the paper is described as follows. In section 2, the governing equations and numerical methods will be introduced briefly. In section 3, the definition of the study cases and the computational set up will be given. In section 4, the computational results of baseline case, unsteady blowing case, and blowing case with a 90^0 screw angle and a 30^0 pitch angle will be presented and analyzed.

2.0 GOVERNING EQUATIONS AND NUMERICAL METHODS

2.1 Governing Equations

The three-dimensional compressible Navier-Stokes equations in generalized curvilinear coordinates (ξ, η, ζ) are written in conservative forms:

$$\frac{1}{J}\frac{\partial Q}{\partial t}+\frac{\partial(E-E_v)}{\partial \xi}+\frac{\partial(F-F_v)}{\partial \eta}+\frac{\partial(F-F_v)}{\partial \zeta}=0 \tag{1}$$

The vector of conserved quantities Q, inviscid flux vector (E, F, G), and viscous flux vector (E_v, F_v, G_v) are defined via

$$Q=\begin{pmatrix}\rho\\ \rho u\\ \rho v\\ \rho w\\ E_t\end{pmatrix},\ E=\frac{1}{J}\begin{pmatrix}\rho U\\ \rho U u+p\xi_x\\ \rho U v+p\xi_y\\ \rho U w+p\xi_z\\ U(E_t+p)\end{pmatrix},\ F=\frac{1}{J}\begin{pmatrix}\rho V\\ \rho V u+p\eta_x\\ \rho V v+p\eta_y\\ \rho V w+p\eta_z\\ V(E_t+p)\end{pmatrix},\ G=\frac{1}{J}\begin{pmatrix}\rho W\\ \rho W u+p\zeta_x\\ \rho W v+p\zeta_y\\ \rho W w+p\zeta_z\\ W(E_t+p)\end{pmatrix},$$

$$E_v=\frac{1}{J}\begin{pmatrix}0\\ \tau_{xx}\xi_x+\tau_{yx}\xi_y+\tau_{zx}\xi_z\\ \tau_{xy}\xi_x+\tau_{yy}\xi_y+\tau_{zy}\xi_z\\ \tau_{xz}\xi_x+\tau_{yz}\xi_y+\tau_{zz}\xi_z\\ Q_x\xi_x+Q_y\xi_y+Q_z\xi_z\end{pmatrix},F_v=\frac{1}{J}\begin{pmatrix}0\\ \tau_{xx}\eta_x+\tau_{yx}\eta_y+\tau_{zx}\eta_z\\ \tau_{xy}\eta_x+\tau_{yy}\eta_y+\tau_{zy}\eta_z\\ \tau_{xz}\eta_x+\tau_{yz}\eta_y+\tau_{zz}\eta_z\\ Q_x\eta_x+Q_y\eta_y+Q_z\eta_z\end{pmatrix},G_v=\frac{1}{J}\begin{pmatrix}0\\ \tau_{xx}\zeta_x+\tau_{yx}\zeta_y+\tau_{zx}\zeta_z\\ \tau_{xy}\zeta_x+\tau_{yy}\zeta_y+\tau_{zy}\zeta_z\\ \tau_{xz}\zeta_x+\tau_{yz}\zeta_y+\tau_{zz}\zeta_z\\ Q_x\zeta_x+Q_y\zeta_y+Q_z\zeta_z\end{pmatrix}$$

where $J=\dfrac{\partial(\xi,\eta,\zeta)}{\partial(x,y,z)}$ is Jacobian of the coordinate transformation between the curvilinear (ξ, η, ζ) and Cartesian (x, y, z) frames, and $\xi_x,\xi_y,\xi_z,\eta_x,\eta_y,\eta_z,\zeta_x,\zeta_y,\zeta_z$ are coordinate transformation metrics. The contravariant velocity components U, V, W are defined as

$$U\equiv u\xi_x+v\xi_y+w\xi_z,\ V\equiv u\eta_x+v\eta_y+w\eta_z,\ W\equiv u\zeta_x+v\zeta_y+w\zeta_z.$$

Q_x, Q_y, Q_z in energy equation are defined as

$$Q_x=-q_x+u\tau_{xx}+v\tau_{xy}+w\tau_{xz}$$

$$Q_y=-q_y+u\tau_{xy}+v\tau_{yy}+w\tau_{yz}$$

$$Q_z=-q_z+u\tau_{xz}+v\tau_{yz}+w\tau_{zz}$$

E_t is the total energy. The components of the viscous stress tensor and heat flux are denoted by $\tau_{xx}, \tau_{yy}, \tau_{zz}, \tau_{xy}, \tau_{xz}, \tau_{yz}$, and q_x, q_y, q_z, respectively.

In the dimensionless form, the reference values for length, density, velocities, temperature, pressure and time are $L, \rho_r, U_r, T_r, \rho_r U_r^2$, and L/U_r respectively. In this study, the free stream parameters are chosen as reference values. The chord length of the airfoil is used the reference length. The dimensionless parameters arise from non-dimensional Mach number M_r, Reynolds number R_e, Prandtl number P_r, and the ratio of specific heats γ, are defined respectively as follows

$$M_\infty = \frac{U_r}{\sqrt{\gamma RT}}, \quad \mathrm{Re} = \frac{\rho_r U_r L}{\mu_r}, \quad \mathrm{Pr} = \frac{C_p \mu_r}{k_r}, \quad \gamma = \frac{C_p}{C_v},$$

where R is the ideal gas constant, C_p and C_v are specific heats at constant pressure and constant volume, respectively. Through out this work, $\mathrm{Pr} = 0.7$ and $\gamma = 1.4$. Viscosity is determined according to the Sutherland's law in dimensionless form

$$\mu = \frac{T^{3/2}(1+S)}{T+S}, \; S = \frac{110.3K}{T_\infty}$$

The governing system is closed by the equation of state.

$$\gamma M_r^2 p = \rho T$$

$$E_t = \frac{p}{\gamma - 1} + \frac{1}{2}\rho\left(u^2 + v^2 + w^2\right)$$

The components of the viscous stress tensor and heat flux in non-dimensional form are as follows:

$$\tau_{ij} = \frac{\mu}{\mathrm{Re}}\left[\left(\frac{\partial u_i}{\partial x_j} + \frac{\partial u_j}{\partial x_i}\right) - \frac{2}{3}\delta_{ij}\frac{\partial u_k}{\partial x_k}\right]$$

$$q_i = -\frac{\mu}{(\gamma-1)M_r^2\,\mathrm{Re}\,P_r}\frac{\partial T}{\partial x_i}$$

2.3 Numerical Methods

The numerical method used in this study has high order accuracy and high resolution. The governing equations are solved using LU-SGS implicit method based on a second order Euler Backward scheme. The sixth-order centered compact difference scheme is used for spatial derivatives. High-order compact filter is employed to reduce numerical oscillations.

In Eq. (1), a second order Euler Backward scheme is used for time derivatives, and the fully implicit form of the discretized equations is given by

$$\frac{3Q^{n+1} - 4Q^n + Q^{n-1}}{2J\Delta t} + \frac{\partial\left(E^{n+1} - E_v^{n+1}\right)}{\partial\xi} + \frac{\partial\left(F^{n+1} - F_v^{n+1}\right)}{\partial\eta} + \frac{\partial\left(G^{n+1} - G_v^{n+1}\right)}{\partial\zeta} = 0. \tag{2}$$

Q^{n+1} is estimated iteratively as:

$$Q^{n+1} = Q^p + \delta Q^p$$

where,

$$\delta Q^p = Q^{p+1} - Q^p$$

At step $p = 0, Q^p = Q^n$; as δQ^p is driven to zero, Q^p approaches Q^{n+1}. The flux vectors are linearized as follows:

$$E^{n+1} \approx E^p + A^p \delta Q^p$$

$$F^{n+1} \approx F^p + B^p \delta Q^p$$

$$G^{n+1} \approx G^p + C^p \delta Q^p$$

So that Eq. (2) can be written as:

$$\left[\frac{3}{2} I + \Delta t J\left(D_\xi A + D_\eta B + D_\zeta C\right)\right]\delta Q^p = R \tag{3}$$

where R is the residual:

$$R = -\left(\frac{3}{2}Q^p - 2Q^n + \frac{1}{2}Q^{n-1}\right) - \Delta t J\left[D_\xi\left(E - E_v\right) + D_\eta\left(F - F_v\right) + D_\zeta\left(G - G_v\right)\right]^p \tag{4}$$

D_ξ, D_η, D_ζ represent partial differential operators, and A, B, C are the Jacobian matrices of flux vectors:

$$A = \frac{\partial E}{\partial Q}, \quad B = \frac{\partial F}{\partial Q}, \quad G = \frac{\partial G}{\partial Q}$$

The right hand side of Eq. (3) is discretized using sixth-order compact scheme (Lele, 1992) for spatial derivatives, and the left hand side of the equation is discretized following LU-SGS method (Yoon, et al ., 1992) In this method, the Jacobian matrices of flux vectors are split as:

$$A = A^+ + A^-, \quad B = B^+ + B^-, \quad C = C^+ + C^-$$

where

$$A^\pm = \frac{1}{2}\left[A \pm r_A I\right], \quad B^\pm = \frac{1}{2}\left[B \pm r_B I\right], \quad C^\pm = \frac{1}{2}\left[C \pm r_C I\right]$$

and,

$$r_A = \kappa \max\left[\left|\lambda(A)\right|\right] + \tilde{\upsilon}, \quad r_B = \kappa \max\left[\left|\lambda(B)\right|\right] + \tilde{\upsilon}, \quad r_C = \kappa \max\left[\left|\lambda(C)\right|\right] + \tilde{\upsilon}$$

where $\lambda(A)$, $\lambda(B)$, $\lambda(C)$ are eigenvalues of A, B, C respectively, κ is a constant greater than 1. $\tilde{\nu}$ is taken into account for the effects of viscous terms, and the following expression is used:

$$\tilde{\nu} = \max\left[\frac{\mu}{(\gamma-1)M_r^2 R_e P_r}, \quad \frac{4}{3}\frac{\mu}{R_e}\right]$$

The first-order upwinding finite difference scheme is used for the split flux terms on the left hand side of Eq. (3). This does not affect the accuracy of the scheme when solutions are converged. As the left hand side is driven to zero, the discretization error will also be driven to zero. The finite difference representation of Eq. (3) can be written as:

$$\begin{aligned}&\left[\frac{3}{2}I + \Delta tJ(r_A + r_B + r_C)I\right]\delta Q^p_{i,j,k} \\ &+ \Delta tJ\left[A^-\delta Q^p_{i+1,j,k} - A^+\delta Q^p_{i-1,j,k} + A^-\delta Q^p_{i+1,j,k} - A^+\delta Q^p_{i-1,j,k} + A^-\delta Q^p_{i+1,j,k} - A^+\delta Q^p_{i-1,j,k}\right] \\ &= R^p_{i,j,k} \end{aligned} \tag{5}$$

In LU-SGS method, Eq. (5) is solved with three steps. First initialize δQ^0 using

$$\delta Q^0_{i,j,k} = \left[\frac{3}{2}I + \Delta tJ(r_A + r_B + r_C)I\right]^{-1} R^n_{i,j,k}$$

In the second step, the following relation is used:

$$\delta Q^*_{i,j,k} = \delta Q^0_{i,j,k} + \left[\frac{3}{2}I + \Delta tJ(r_A + r_B + r_C)I\right]^{-1} \Delta tJ\left[A^+\delta Q^*_{i-1,j,k} + B^+\delta Q^*_{i,j-1,k} + C^-\delta Q^*_{i,j,k-1}\right]$$

For the last step, δQ^p is obtained by

$$\delta Q^p_{i,j,k} = \delta Q^*_{i,j,k} - \left[\frac{3}{2}I + \Delta tJ(r_A + r_B + r_C)I\right]^{-1} \Delta tJ\left[A^-\delta Q^p_{i+1,j,k} + B^-\delta Q^p_{i,j+1,k} + C^-\delta Q^p_{i,j,k+1}\right]$$

The sweeping of the computational domain is performed along the planes of $i + j + k = const$, i.e. in the second step, sweeping is from the low-left corner of the grid to the upper-right corner, and then vice versa in the third.

Parallel computing based on Message Passing Interface has been utilized to improve the performance of the code. The parallel computing is combined with the domain decomposition method. The computational domain is divided into n equal-sized sub-domains along ξ direction which is usually the streamwise direction. The details of the numerical methods and parallel computing can be referred to (Jiang, et al, 1999; Jiang, et al, 1999; Shan, et al, 2001).

3.0 PROBLEM DEFINITIONS AND BOUNDARY CONDITIONS

Numerical simulations are performed on a NACA0012 airfoil at attack angle of 4^0. The free stream velocity U_∞, pressure p_∞, temperature T_∞ and chord length of the airfoil C are selected as the reference velocity, pressure, temperature and length respectively, which are used to non-dimensional governing equations. The computational domain is plotted in Figure 3.1. The upstream boundary is 3 chord lengths away from the leading edge of the airfoil. The upper and lower boundaries are about 4 chord lengths from the solid surface. The outflow boundary is 2 chord lengths downstream of the trailing edge. The airfoil is regarded as infinite in the spanwise direction. In our simulation, the spanwise length is set as $L_y = 0.1C$, and periodic boundary condition is imposed at the spanwise boundaries.

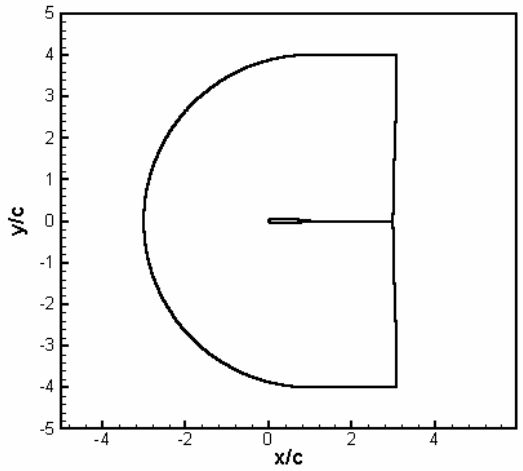

Figure 3.1 Computational domain

The flow and computational conditions are listed in Table 1. The Reynolds Number based on free stream velocity and chord length is $R_e = 10^5$. The free stream Mach Number is $M_a = 0.2$. The numbers of grid points in ξ, η, ζ directions are $N_x = 1200$, $N_y = 32$, $N_z = 180$ respectively. Grid distributions in the (x, z) plane and on the airfoil surface are shown in Figure 3.2. Grids are uniform in the spanwise direction and stretched in the wall-normal direction. C-grid is used in the (x, z) plane. The grid sizes in wall unit are also listed in Table 1. Parallel computation is based on the domain decomposition. The computational domain is divided evenly into N sub-domains along the ξ direction when N processors are used. In this work, 24 processors are used for all cases.

Table 1. Flow and computational conditions

$\mathrm{Re}=U_\infty C/\upsilon_\infty$	M_∞	AOA	$N_x \times N_y \times N_z$	Δx^+	Δy^+	Δz^+
10^5	0.2	4^0	$1200\times32\times180$	<13	<15	<1

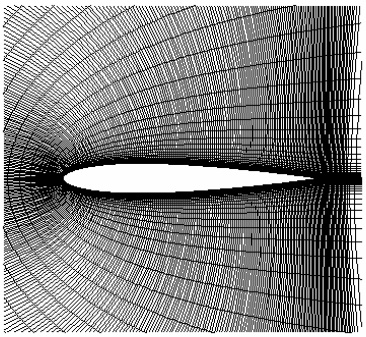

(a) Grid in (x, z) plane

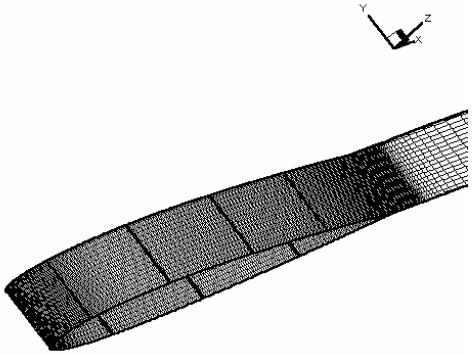

(b) Grid on the airfoil surface

Figure 3.2 Grid distribution (one out of three grid point is shown)

As the flow is subsonic in the free stream, the uniform free stream velocities and temperature are prescribed at upstream and far field boundaries. Then density is decided by non-reflecting boundary condition developed in our previous work (Jiang, et al, 1999). Non-slip, adiabatic boundary condition is used on the wall surface of the airfoil. Non-reflecting boundary condition is applied to the outflow boundary.

4.0 RESULTS AND ANALYSIS

To study the separation and transition processes on the airfoil and the effects of different types of blowing on separation and transition, we set up four cases: I. Baseline case without blowing; II. Steady blowing; III. Pulsed blowing; IV. Blowing jet with a 30^0 pitch angle and a 90^0 screw angle.

All simulations are carried out with a time step equal to $8.35\times10^{-5}C/U_{\infty}$. The corresponding CFL number is around 400.

4.1 Flow around the airfoil without blowing (Baseline Case)

Case I is the baseline case without blowing. 2D solutions are used as the initial field. For this case, the time integration has reached $t = 3.474C/U_\infty$. Mean values are obtained by performing averaging in the spanwise direction and in time over a period of $3C/U_\infty$.

4.1.1 2D instability waves and vortex shedding

2D instability waves and vortex shedding appear in both 2D and 3D simulations. The generation and growing of 2D instability waves is the initial stage of the transition. In 2D simulation, due to lack of 3D motions, we can not see the late stages of the transition and breakdown. But the 2D simulation can provide us important information on how the instability waves develop and grow. 2D simulation starts from a uniform flow field. This initial field is not the solution of the governing equations and may bring in some disturbances (initial disturbance brought by the numerical initial conditions). When perturbations introduced by the initial field can not be dissipated through the time integration, they may trigger the most unstable modes. This is the reason why we see unsteady behaviors in the simulation although all boundary conditions are steady and no external disturbances are introduced. Flow separation and vortex shedding appear on the suction surface of the airfoil (Figure 4.1.1), where a separated mixing layer and vortex shedding are clearly demonstrated by plotting contours of instantaneous spanwise vorticity. The separation zone can be seen clearly from the time averaged velocity vectors shown in Figure 4.1.2. The 2D solutions are well developed and quasi-periodic behavior is built up. It can be seen clearly that the boundary layer separates from the airfoil surface and develops to unstable shear layer which leads to the vortex shedding. These large vortex structures travel downstream along the airfoil surface. There is no vortex breakdown observed in the 2D simulation since the breakdown is a 3-D and non-linear interaction. This shows 2D direct numerical simulation can only predict early instability stages, but cannot reveal the transition and flow control mechanism.

Figure 4.1.1 Contours of spanwise vorticity from 2D solution

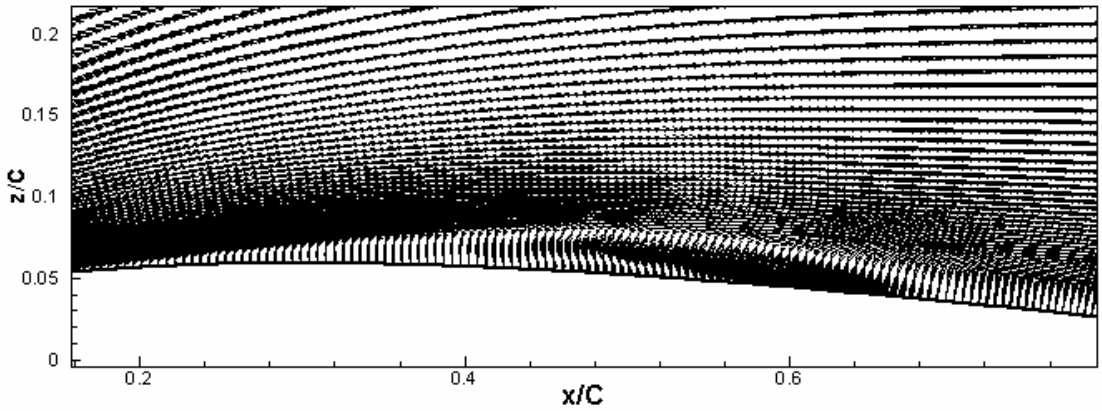

Figure 4.1.2 Time averaged velocity field

Note that we did not add any disturbance at inflow, there is a question raised what kind of disturbance triggers the instability wave inside the separated free shear layer? Figure 4.1.3 shows time history of fluctuation pressure at different locations. We can see that pressure fluctuating appears first at $x/c = 1.048$ which is located in the wake close to the trailing edge (wake instability). As we mentioned before that the disturbances introduced by initial field may excite the most unstable instability wave. From the simulation results, we find that large pressure oscillations appear first in the wake close to the trailing edge. It is because wake is generated by a free shear layer with inflection points but without any solid wall nearby unlike the boundary layer or separated shear layer, which makes the wake most unstable. The time dependent behaviors of streamwise velocity at different streamwise locations are given in Figure 4.1.4, which also confirms that the wake becomes unstable first.

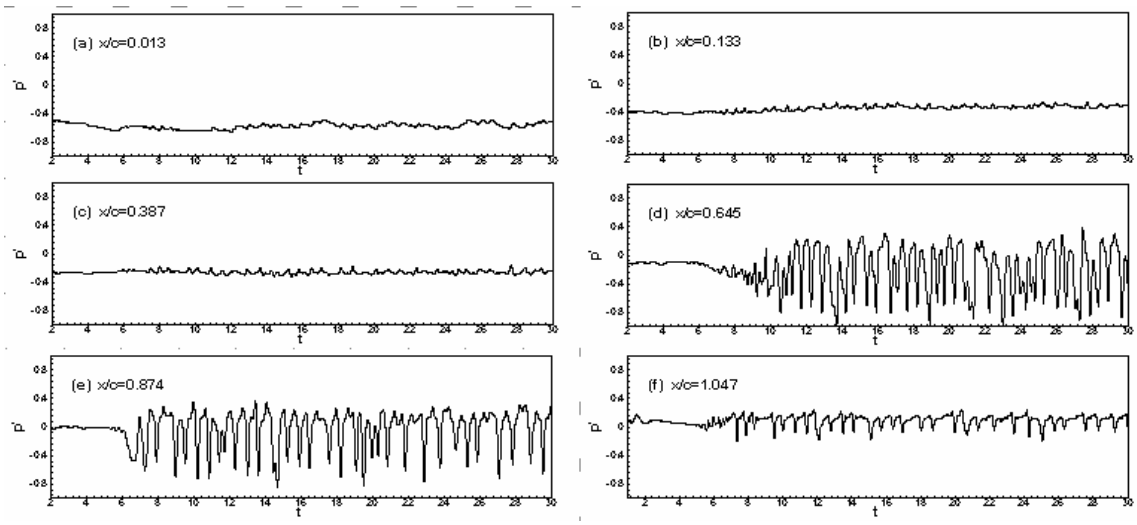

Figure 4.1.3 Time history of pressure fluctuation at different locations

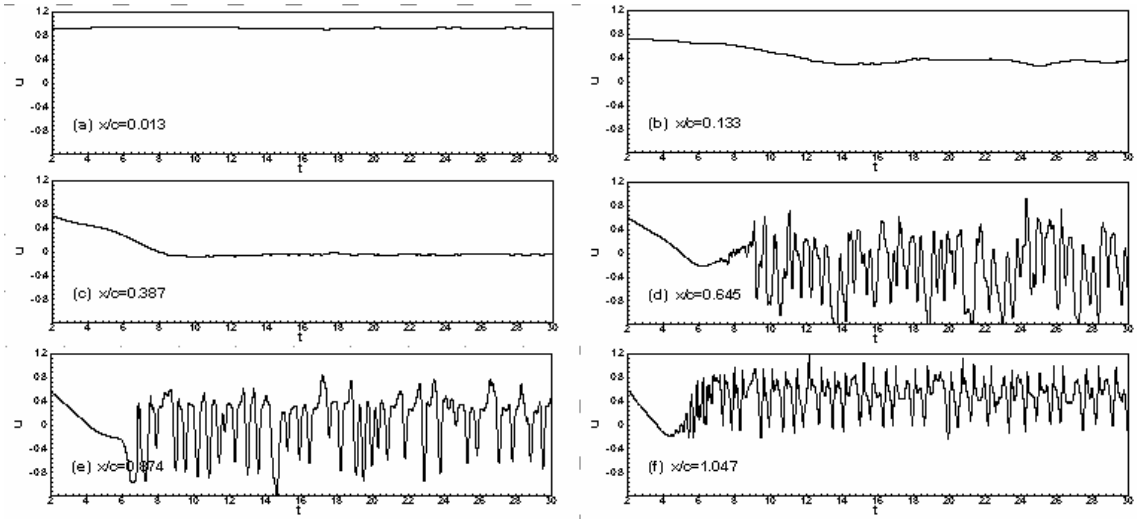

Figure 4.1.4 Time history of streamwise velocity at different locations

Then disturbances generated in wake near the trailing edge propagate upstream through acoustic waves. These upward traveling disturbances could change the pressure distribution on the surface. Then, the separation point and the stagnation point become unstable (we call it 'stagnation instability'). The disturbances generated at these locations convect downstream inside the separated shear layer as vortical disturbances. The shear layer has inflected profile with strong reverse flow which subjects to inviscid shear layer instability with much larger growth rate than the viscous counterpart. Figure 4.1.5 shows the profiles for the mean streamwise velocity at different locations. Some DNS results shows that the shear layer has absolute instability when backflows are as high as 15-20% of the external velocity (Yang & Voke, 2001). From Figure 4.1.5 we can see that the reverse velocity reaches 8% of the freestream velocity at $x/C = 0.4$, which is below the absolute instability range, but at this point we still can see obvious unsteadiness. The disturbances are rapidly amplified in the shear layer and develop to shed vortex structures. Many authors have related this instability mechanism to the Kelvin-Helmoholtz instability. The condition for the Kelvin-Helmoholtz instability to occur is $0 < Kh < 1.2785$ (Yang & Voke, 2001) where K is the wave number and h is the shear layer thickness. In the present simulation, unsteadiness becomes obvious at about $x/C = 0.4$, where the shear layer thickness is about $h \approx 0.0202C$ and the wavelength is $\lambda \approx 0.115C$. Then we get $Kh = \frac{2\pi}{\lambda} h \approx 1.104$, which satisfies the criteria for the Kelvin-Helmoholtz instability to develop.

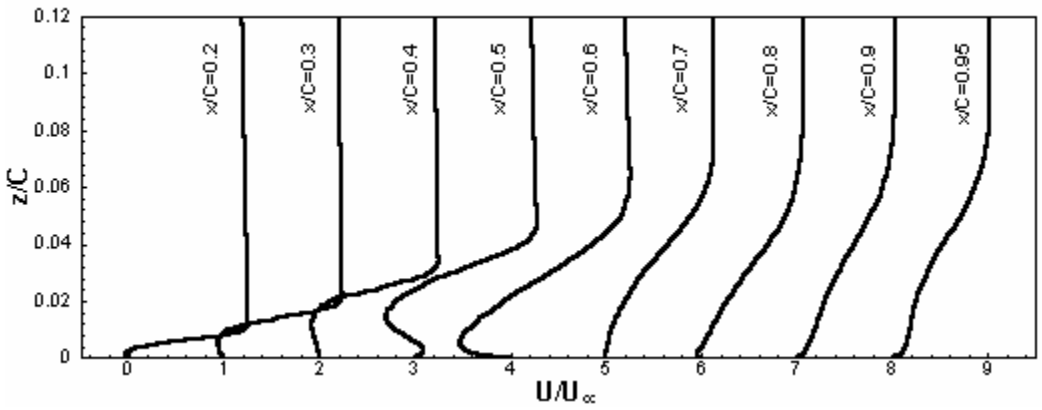

Figure 4.1.5 Mean velocity profiles at different locations

Figure 4.1.6 shows the spectrum of pressure waves at the location close to the wall. The spectrum at different streamwise locations from the leading edge to the trailing edge shows the strong peak at the frequency around $F^+ = 1.4$, which is about the vortex shedding frequency (vortex shedding frequency is changing from time to time). There is a peak at $F^+ \approx 0.3$ which may correspond to so-called low-frequency flapping. As the flow is subsonic, acoustic waves travel in both upstream and downstream directions. The pressure field is dominated by the vortex shedding frequency, which is also the frequency of Kelvin-Helmoholtz instability wave. This may provide a clue for flow control that the blowing jet for separation control should have same or similar frequency with a very little mass flow (sharp shape in both time and space). This will be discussed later. When disturbances grow large, nonlinear interactions take place. We can see more high frequencies appear in the spectrum.

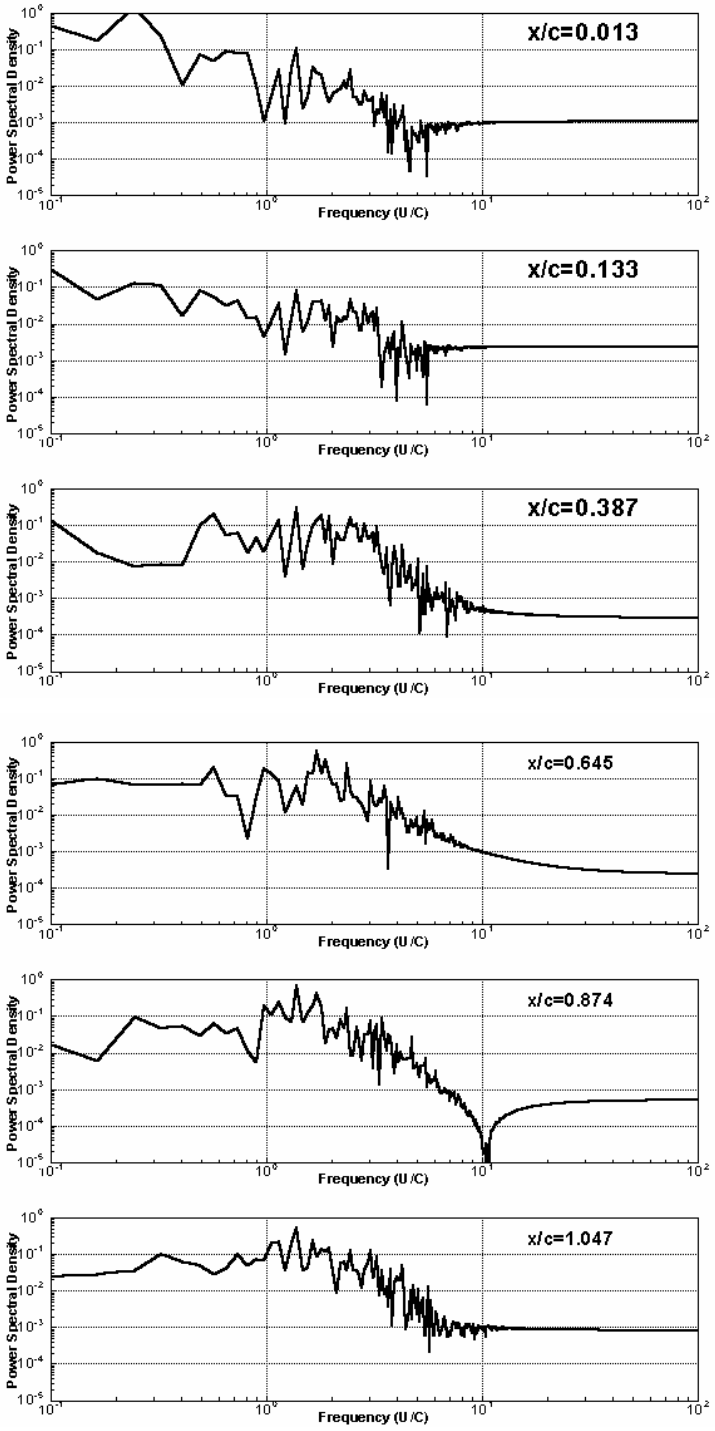

Figure 4.1.6 Power spectral density of pressure at the mid-boundary layer

4.1.2 Mean flow

3D solutions are highly unsteady. Mean flow characteristics are analyzed first. Figure 4.1.7 shows the maximum reverse flow in the wall normal direction along the suction surface. The separated zone appears form $x/C = 0.19$ to $x/C = 0.68$, where the separated laminar boundary evolves into reattached turbulent boundary layer. The reverse flow reaches 8% of the free stream velocity at about $x/C = 0.5$. After that the reverse flow appears to be much stronger. From velocity vectors which are plotted in Figure 4.1.8, the separation zone can be identified clearly. The reversed flow is very strong near the end of the separation zone.

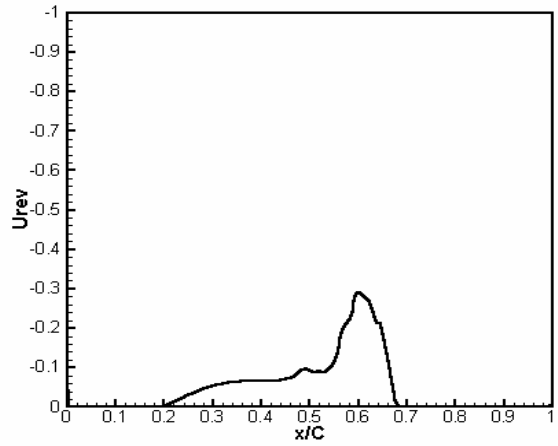

Figure 4.1.7 Mean reverse flow distribution on the suction side, $U_{rev} = \min(\overline{u})$

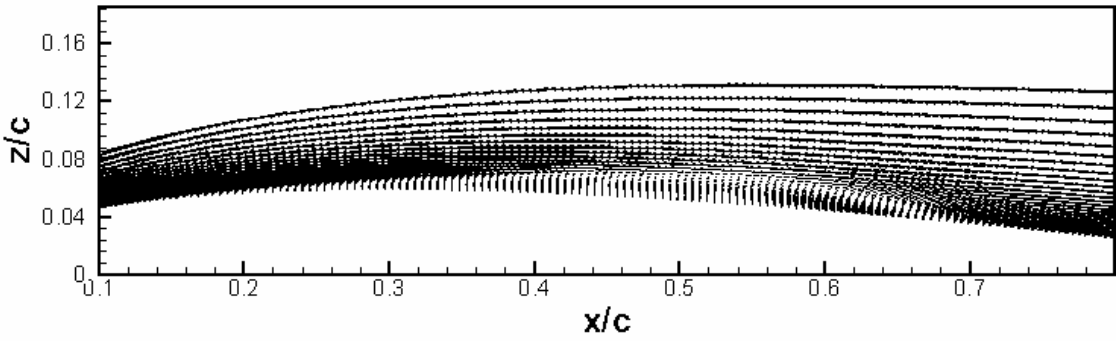

Figure 4.1.8 Mean velocity vector

Figure 4.1.9 shows the mean pressure coefficient. The flattened region indicates the separation of the boundary layer. The strong adverse pressure gradient at the fore part of the suction surface causes the boundary layer to separate from the surface. In the separation zone, the adverse pressure gradient is reduced dramatically. Near the end of the separation zone, large adverse pressure gradient forms again and leads to a rapid increase of the reversed flow which is clearly demonstrated in Figure 4.1.7. Figure.4.1.10 shows the skin friction coefficient of the suction surface. The skin friction increases when the transition happens. The

separated shear layer becomes turbulent and reattaches to the airfoil surface, forming a closed bubble. As the flow is very unsteady, the shape and the length of the bubble are changing from time to time in a large scale. The time averaged length of bubble is about $l_b / C = 0.48$ which can be estimated from Figure 4.1.7. After the reattachment, the skin friction coefficient grows rapidly to a high value within a short distance, and then stay close to that level with some oscillations which are caused by large vortex structures.

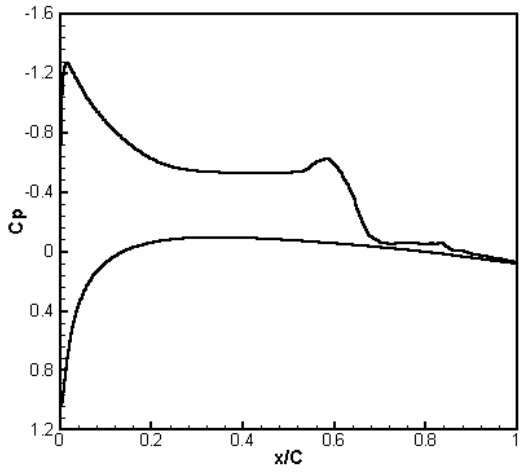

Figure 4.1.9 Mean pressure coefficient

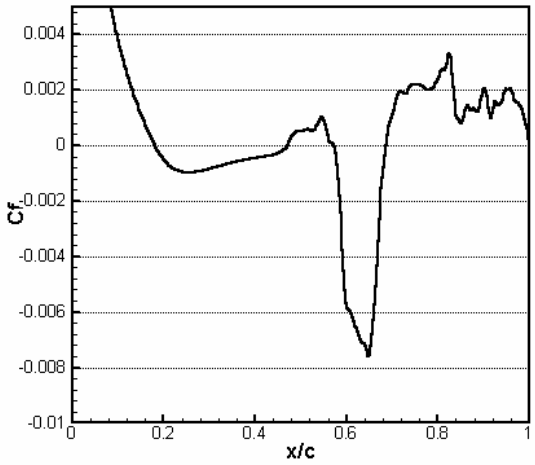

Figure 4.1.10 Mean skin friction coefficient

In this simulation, no external disturbance is introduced, but we observed the growth of the disturbance, instability waves and transition. We have discussed in the 2D scase that according to our observation, the acoustic waves generated near the trailing edge travel upstream, which could change the pressure distribution on the airfoil surface. The stagnation point and the separation point are closely related to the pressure distribution and can be unsteady if the pressure distribution changes. The disturbances generated at these points are convected downstream. The separated shear layer is very unstable. The disturbances convected in

the shear layer are amplified rapidly. The detached shear layer becomes unstable via the Kelvin-Helmholtz mechanism. Figure 4.1.11 shows the maximum the r.m.s. values of fluctuation velocities across the boundary layer along the surface. The growth of disturbances can be seen clearly. Before the separation point at $x/C = 0.19$, u' and w' are small but not zero, which indicate that small 2D disturbances exist. The disturbances inside the boundary layer start to growth before the separation point (viscous instability) at around $x/C = 0.2$. Then the disturbance grows in a much faster rate in the separated shear layer corresponding to the inviscid instability at $x/C = 0.2 - 0.4$. u' increases rapidly at about $x/C = 0.4$, where the reversed flow reaches 8% of the free stream velocity. This strong reversed flow makes the shear layer very unstable and leads to the sudden rapid growth of disturbances. Following the sudden growth of u', w', spanwise velocity also starts to grow. The velocity fluctuations reach a maximum value before the mean reattachment point. The rapid growth of velocity fluctuations indicates the appearance of three dimensional motion and nonlinear interaction which leads to breakdown and turbulence. After the breakdown, the separated shear layer reattaches on to the surface and becomes an attached turbulent boundary layer.

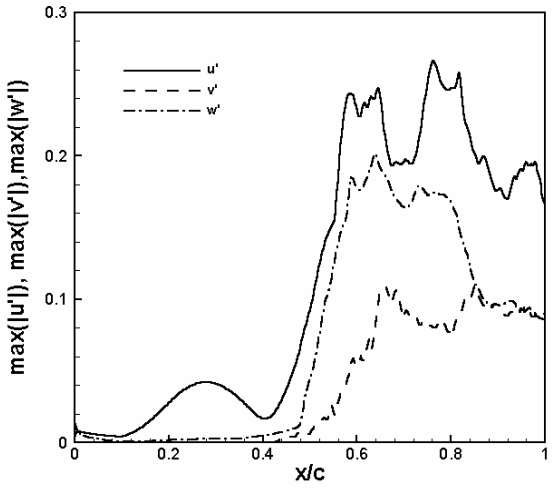

Figure 4.1.11 Peak r.m.s across the boundary layer

The mean velocity profiles, the r.m.s fluctuation velocity profiles, and the Reynolds stress are depicted in Figure 4.1.12 (a) (b) (c) respectively. In the separation zone, mean velocity profiles demonstrate inflected shapes. After the reattachment, the boundary layer develops to the turbulent velocity profile. The r.m.s fluctuation of the streamwise velocity profiles at different locations are displayed in (b) which clearly shows the maximum fluctuation happened in the separated shear layer away from the solid surface in normal direction corresponding to the invisid instability which is much larger than the viscous instability near the solid surface. The first location ($x/C = 0.2$) is very close to the separation point. The peak appears at about the center of the boundary layer. At the following two locations, the fluctuations grow and two peaks show up. From $x/C = 0.5$, the fluctuations grow rapidly and three peaks are found at some locations. This evolution is related to the amplification of the upstream perturbations due to the existence of the inflected velocity profile (invisid instability), vortex shedding and prime vortex breakdown. Profiles of Reynolds stress are shown in (c). Peak values appear inside the boundary layer.

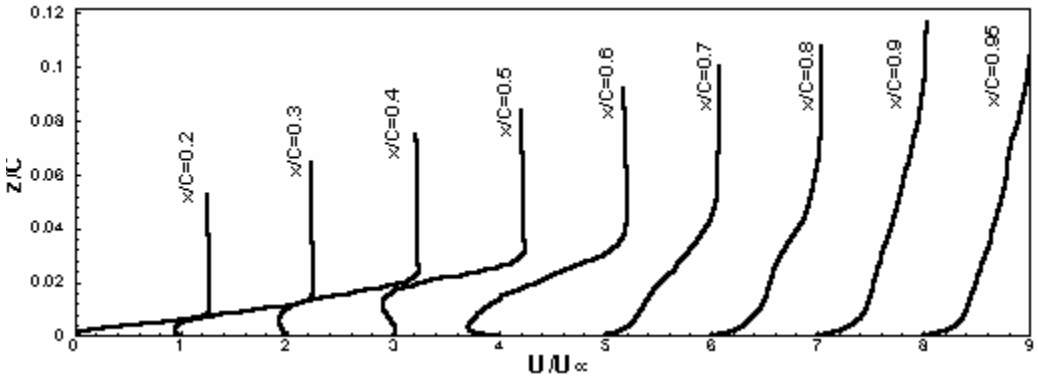

(a) Mean streamwise velocity profiles

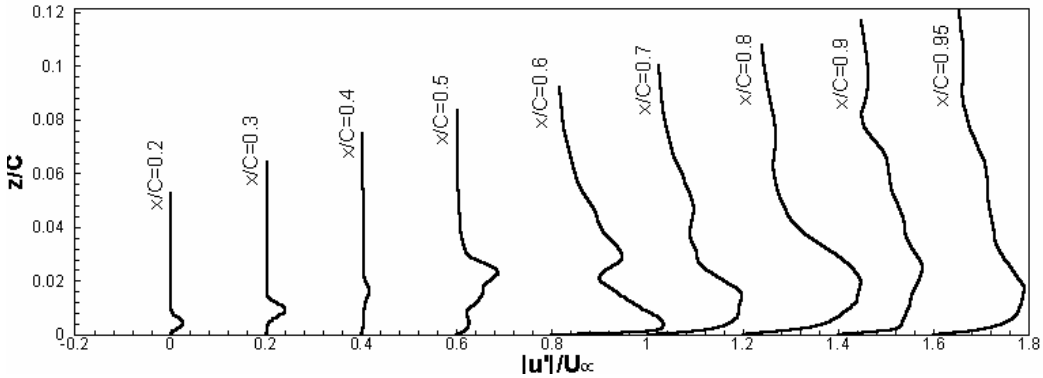

(b) The r.m.s streamwise fluctuation velocity profiles
(Maximum fluctuation happens in the separated shear layer)

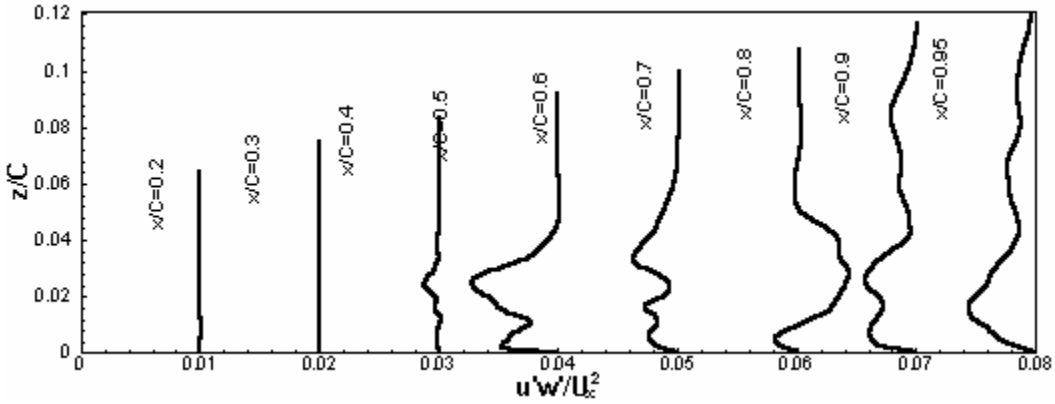

(c) Reynolds stress $\overline{u'w'}$

Figure 4.1.12 Statistic profiles

4.1.2 Instantaneous characteristics

Figure 4.1.13 shows the contours of the instantaneous spanwise vorticity in the middle (x, z) plane. As the 3D simulation is started from the 2D solutions, the vortex evolution and breakdown can be clearly seen from these time sequent pictures. Before the 3D flow is fully built up, instability waves growing in the shear layer and corresponding vortex shedding can be clearly identified. When the run time for the 3D simulation is long enough, real 3D motion is fully developed. Nonlinear interactions of velocity fluctuations become very strong and lead to rapid fluctuation growth. Compared with the 2D solution in Figure 4.1.1, the organized vortex shedding disappears and vortex breakdown ccurs in a very short distance. It is also shown that the 2-D simulation cannot catch the physics for either the flow separation and transition or flow control. The 2-D mechanism is different from the 3-D mechanism and the 3-D simulation has to be conducted for flow separation, transition, and control.

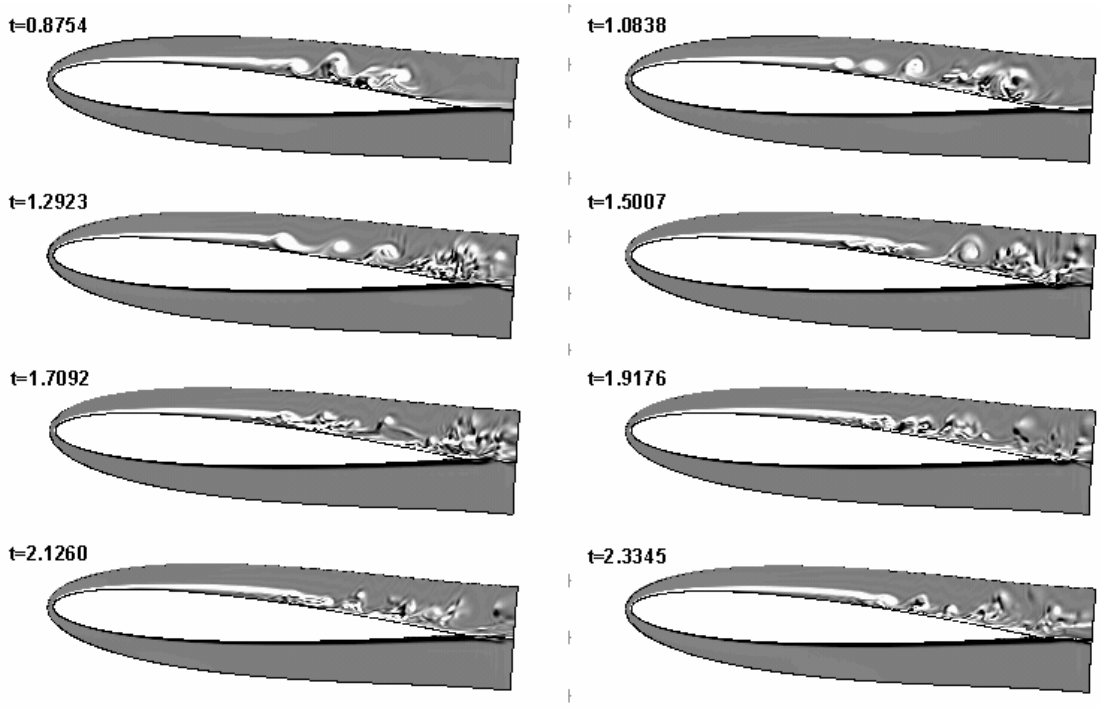

Figure 4.1.13 Instantaneous spanwise vorticity at different time

The iso-surfaces of instantaneous vorticity in three directions are plotted in Figure 4.1.14. The transition process and breakdown of the rolling-up shear layer are clearly demonstrated in (b). The vortex shed from the separated shear layer are distorted while traveling downstream. The spanwise vorticity iso-surface becomes rippled when the 3D vortex appears. Streamwise vortices and wall-normal vortices are shown in (a) and (c) respectively. The interactions of 3D structures cause spanwise vorticity iso-surface to break into small pieces, indicating the breakdown of vortices occurs. The boundary layer becomes fully turbulent after reattachment. During the transition process, the instability wave grows rapidly and is companied by the appearance of the three-dimensional motions which leads to the breakdown of the boundary layer.

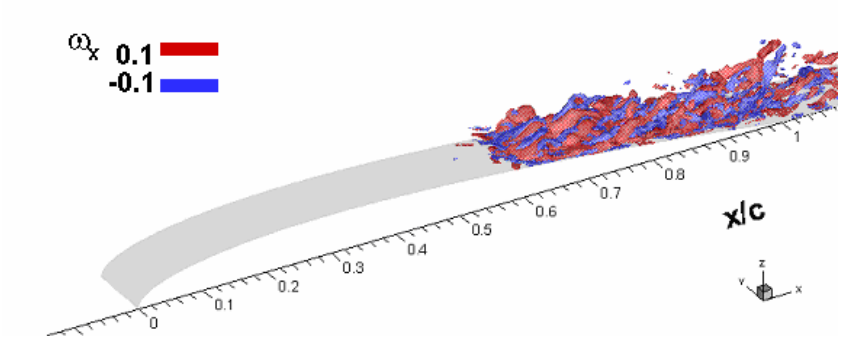

(a) streamwise vorticity

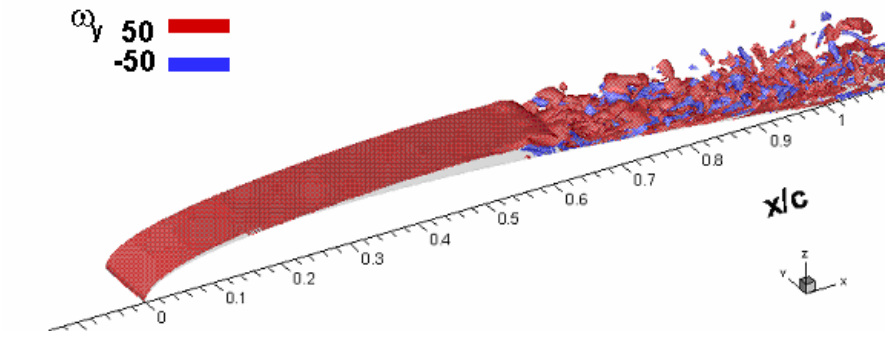

(b) spanwise vorticity

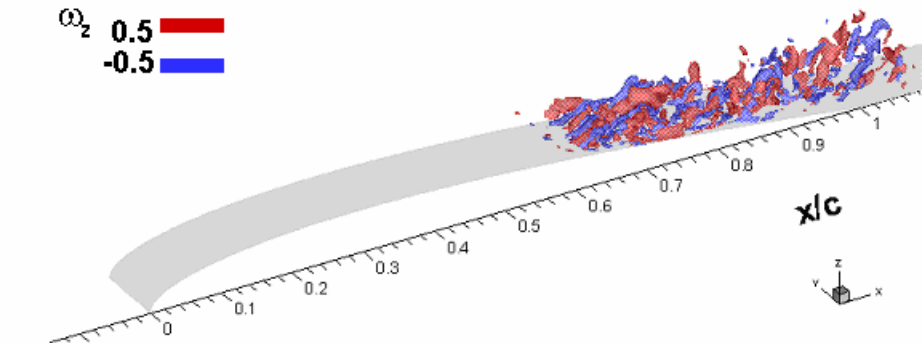

(c) wall-normal vorticity

Figure 4.1.14 Iso-surface of instantaneous vorticity

From the graphic (Figure 4.11.13) and movie made with DNS data, we can find the shed vortex is quickly deformed and stretched. The core of the prime vortex is faded due to dissipation and a negative vortex beside the prime vortex is induced by the prime vortex and, eventually, the prime vortex breaks down to small pieces

corresponding to the flow transition to turbulence. From the 3-D graphic (Figure 4.11.14), the vortex structure clearly shows the stremwise and spanwise wortex interaction and a λ - shape vortex developed, rolls up, and breaks down. From Figure 4.11.14, we can find the streamwise vortex plays a key role in the transition process. Whenever the streamwise vortex appears, the vortex rolls up and breaks down quickly. There is a remaining question, where is the stremwise vortex from since there is no 3-D external perturbation added? The possible way could be 3-D acoustic waves from the wake (wake instability is 3-D dimensional) or 3-D motion of the shed prime vortex.

Figure 4.1.15 shows streamwise evolutions of the vorticity extrema. $\omega_x, \omega_y, \omega_z$ denote vorticity component in the streamwise, spanwise and wall-normal directions respectively. The solid lines correspond to maximum values, the dashed lines to minimum values. The streamwise and wall-normal vorticity components remain almost zero up to transition. Downstream, the minimum and maximum vorticity oscillates seriously, showing a symmetrical pattern. The spanwise vorticity component has large value close to the leading edge and remains at a lower level after the separation. Oscillation appears when transition starts.

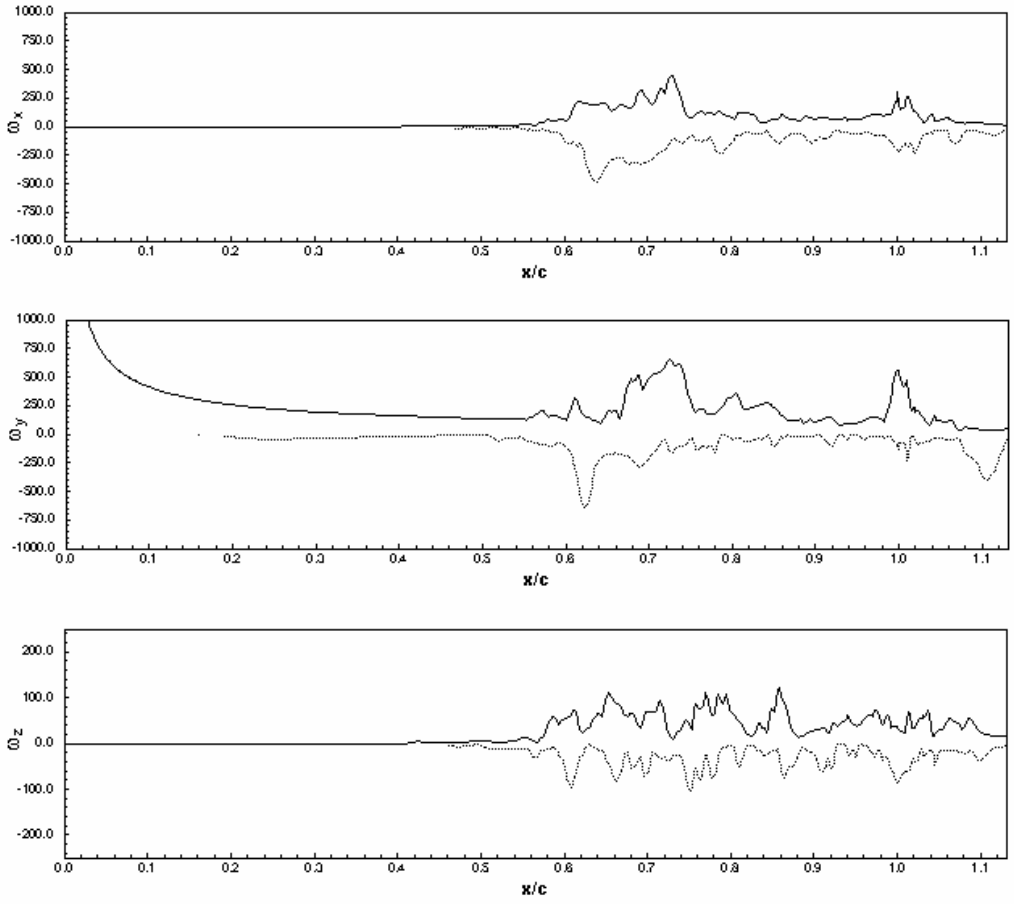

Figure 4.1.15 Instantaneous extrema of vorticity

Power spectral density of the streamwise velocity at mid-boundary layer is given in Figure 4.1.16. Peaks at low frequencies are located at $F^+ = 1 \sim 2$, as we discussed in the 2D section, corresponding to the Kelvin-Helmoltz instability wave and vortex shedding. Stronger peaks at higher frequencies appear gradually further downstream as a result of nonlinear interactions. During and after the transition, energy peaks appear over a wide band of frequency.

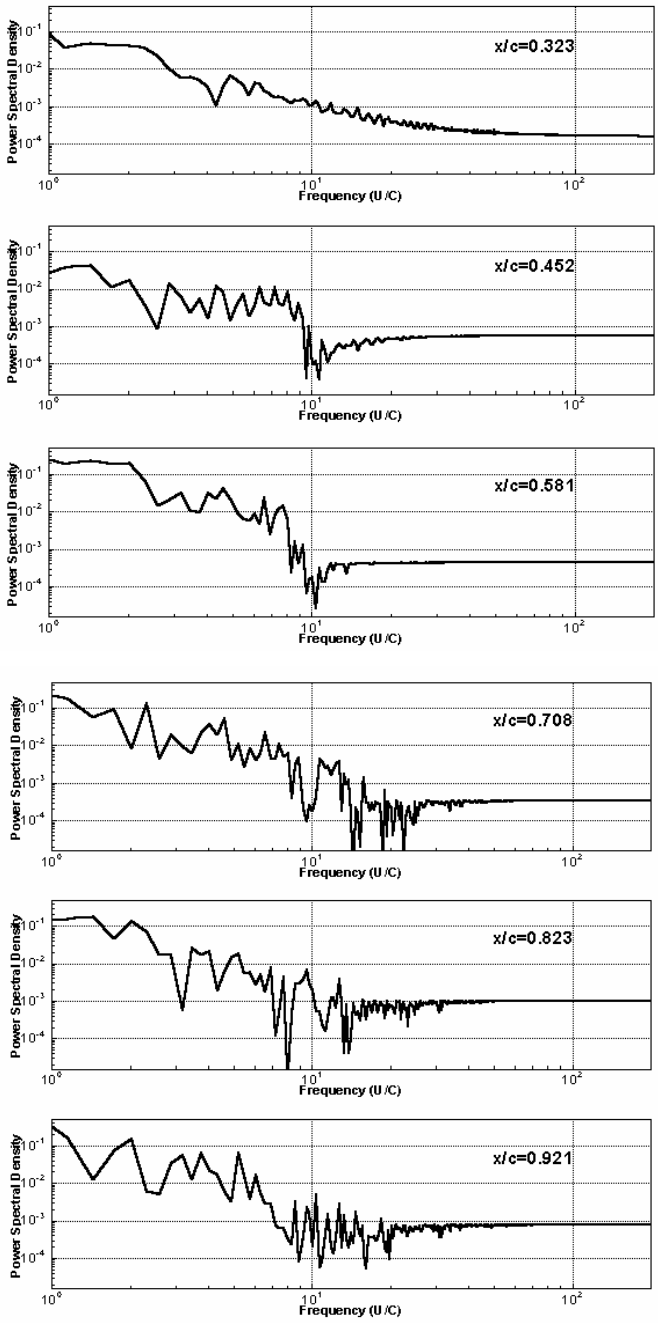

Figure 4.1.16 Power spectral density of streamwise velocity

This baseline case study indicates that the transition to turbulence will reattach the separated boundary layer. Though no external disturbances are introduced, the initial perturbations come from the up-ward traveling acoustic waves which are generated in the wake. The separation points and the stagnation point are closely related to the pressure distribution on the airfoil surface. The upward traveling acoustic waves may affect the pressure distribution which further changes the separation points and stagnation points. This oscillation introduces perturbations inside the boundary. The perturbations are convected downstream as vortical disturbances. The separated shear layer is very unstable when the reversed flow is large enough. The traveling disturbances trigger instability waves inside the shear layer. The appearance of 3D motions and nonlinear interactions of disturbances after the vortex shedding leads to the sudden growth of the disturbances and breakdown. The shear layer becomes turbulent and reattaches to the wall surface. This process is then further sustained by the global feed back mechanisms. This analysis leads to the conclusion that reattachment takes place right after the transition, which provides a clue for flow separation control. In order to prevent separation or reduce separation zone, we can use external disturbance to trigger the early transition. When unsteady blowing is used in flow separation control, the disturbance introduced by unsteady blowing will excite the inherent local instability wave and lead to early transition to turbulence which will reduce the separation zone by early reattachment of the separated shear layer or late separation of the boundary layer. The frequency of the unsteady blowing and the length of the blowing hole provide the frequency and wave length scales for picking up the most unstable modes.

4.2 Flow around the airfoil with a pulsed blowing jet

Based on above observations and analysis, we set up two cases (actually three cases, but the steady blowing has similar results as the pulsed jet with more mass flow and, therefore, is not reported here) to investigate how the blowing jet (vortex generation jet or VGJ) affects the transition process. All flow parameters and geometry are the same as in baseline case except for that blowing is introduced on the suction side of the airfoil. The unsteady blowing is enforced from $x_0 = 0.153$ to $x_1 = 0.175$, which is before the separation point $x_s = 0.19$. The non-dimensional frequency of blowing $F^+ = FC/U_\infty$ is set to be 2 (we now believe 1.4 is a better choice), where C is the chord length and F is the frequency. The blowing velocity has 90^0 pitch angle and 0^0 screw angle. Pitch angle is defined as the angle the jet makes with the local surface and skew angle is defined as the angle of the projection of the jet on the surface relative to the local free-stream. With this configuration, the blowing velocity is set in the wall-normal direction. The blowing velocity is given as follows,

$$w(x,y,t) = Af(x,y)\exp[-k(\frac{2\tau}{T}-1)^2]$$

where,

$$f(x,y) = [0.5-0.5\cos(\theta_x)][0.5-0.5\cos(\theta_y)]$$

$$\theta_x = 2\pi\frac{x-x_0}{x_1-x_0}, \quad \theta_y = 2\pi\frac{y}{L_y}, \quad \tau = t-nT, \quad T = 1/F^+, \quad A = 0.4, \quad k = 12$$

Shape functions in space and time which are used to define spatial distribution and temporal variation of the blowing velocity are depicted in Figure 4.2.1. $k = 12$ is used in this case. This parameter can be used to control blowing mass.

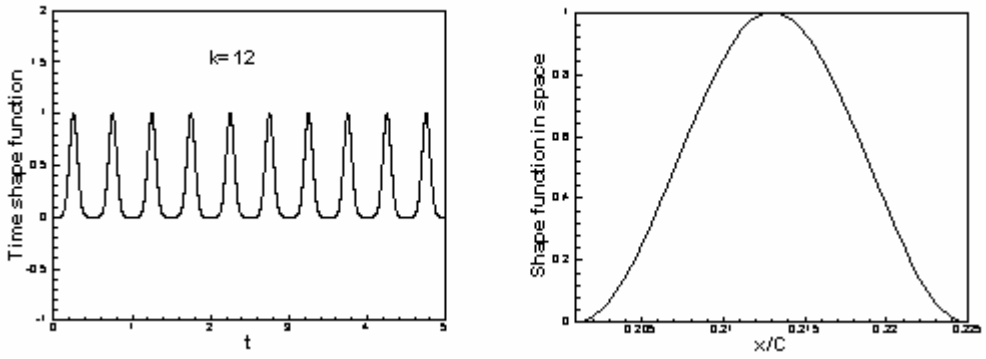

Figure 4.2.1 Shape functions in time and space

The time integration for unsteady blowing case has reached $t = 3.73C/U_\infty$. Time averaging is performed over four periods of blowing. Mean velocity vectors are shown in Figure 4.2.3. It is obvious that large separation zone which is clearly seen in the baseline case shown in Figure 4.1.4 is dramatically reduced (almost removed). When we look at streamwise mean velocity profiles of the baseline case (Figure 4.1.7) and blowing case which are shown in Figure 4.2.4, we can find that the reversed flow completely disappear after $x/c = 0.4$ and boundary layer becomes reattached to the surface afterwards.

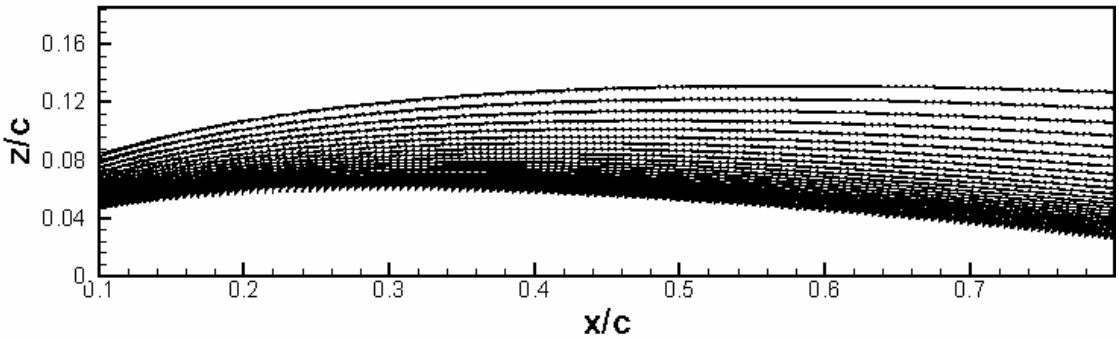

Figure 4.2.3 Mean velocity vectors

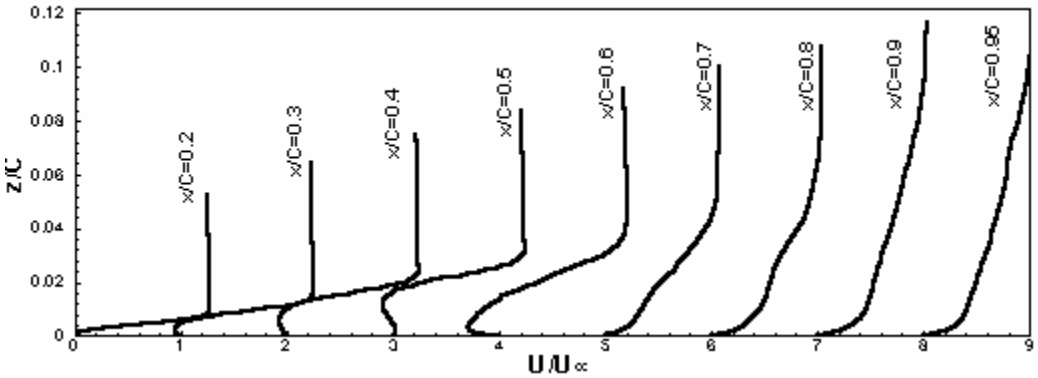

(a) base line case

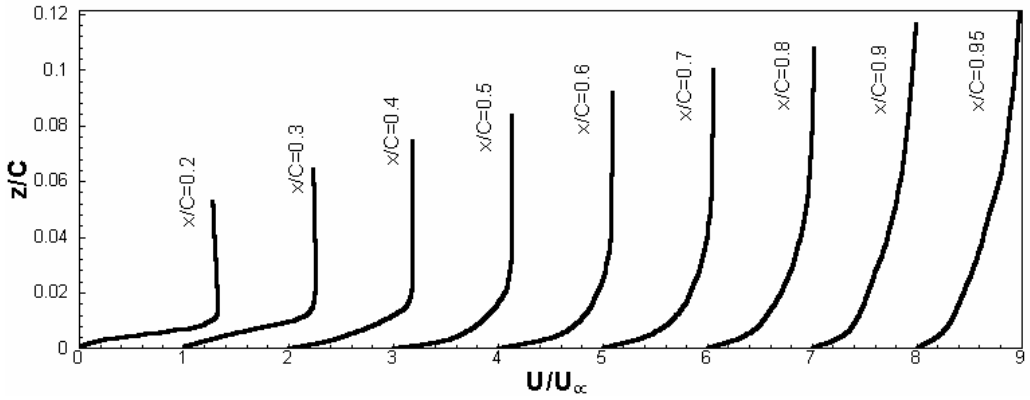

(b) blowing case

Figure 4.2.4 Streamwise mean velocity profiles

The reduced separation zone can also been seen from Figure 4.2.5 in which the maximum reverse velocity is depicted against streamwise location. Under the effect of blowing, the reversed flow appears in very short distance from $x/c = 0.2 \sim 0.3$. Compared with Figure 4.1.3, the reverse flow quickly reaches the maximum value which is about 7% of free stream velocity. While in the baseline case, the reverse flow velocity gradually increases and reach maximum of about 30% free stream velocity. This difference affects the growth of disturbances which will be discussed later. The distribution of mean pressure coefficient is plotted in Figure 4.2.4. As the separation zone is reduced, the flattened area no longer exists. Obviously, this pressure coefficient distribution will not improve the lift force. Temporal variations of lift and drag coefficients which are averaged over spanwise direction are shown in Figure 4.2.5. For our case, the reduction of the separation zone reduces both drag and lift forces.

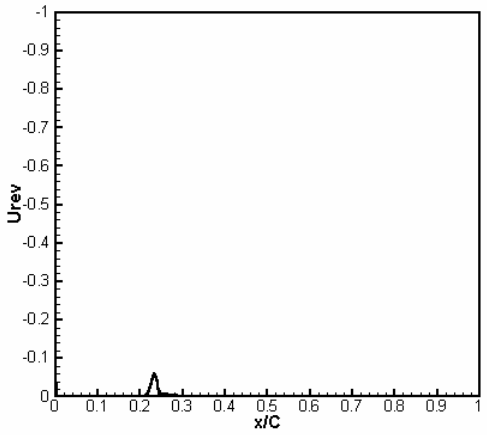

Figure 4.2.3 Mean reverse flow distribution on the suction side, $U_{rev} = \min(\overline{u})$

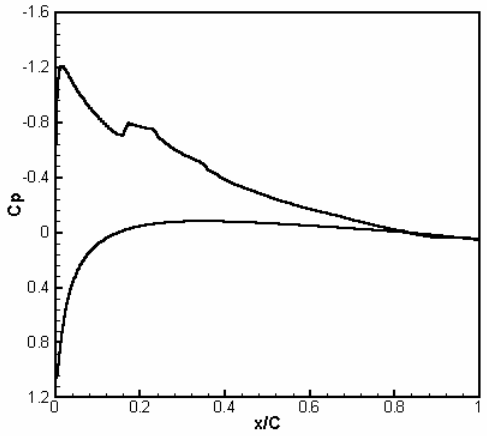

Figure 4.2.4 Mean pressure coefficient

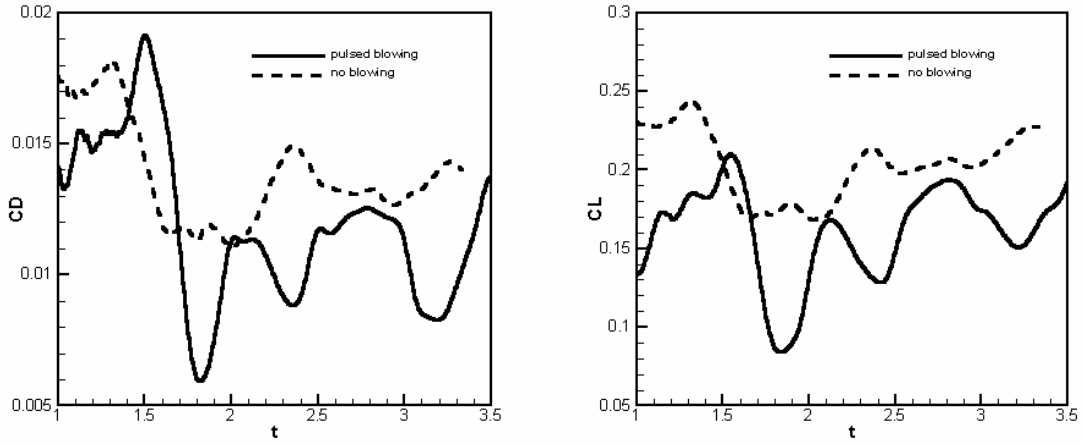

Figure 4.2.5 Temporal variations of lift and drag coefficients

The skin friction coefficient distribution on the suction side is shown in Figure 4.2.6. Figure 4.2.7 shows the peak r.m.s of the velocity fluctuations. In the separation zone, the skin friction coefficient is negative. Around $x/c = 0.4$, there is a rapid growth of the skin friction, indicating the transition to turbulence occurs. As discussed before, there are disturbances coming from the leading edge. The rapid growth of streamwise and wall normal velocity fluctuations starts after the blowing injection point. After a very short distance, they reach a steady level. The growth rate of the spanwise velocity is more rapid than in baseline case. The spanwise velocity fluctuation reaches a stable level around the reattachment point $x/c = 0.4$. In this case, the transition takes place in very short distance and disturbance level is much lower than in the baseline case. Figure 4.2.8 shows the r.m.s streamwise fluctuation velocity profiles at different x-locations. Inside the separation zone, from $x/c = 0.2 \sim 0.4$, peak values can be seen inside the boundary layer, indicating the development of the instability waves. After reattachment, this multi-peak profiles no longer exist.

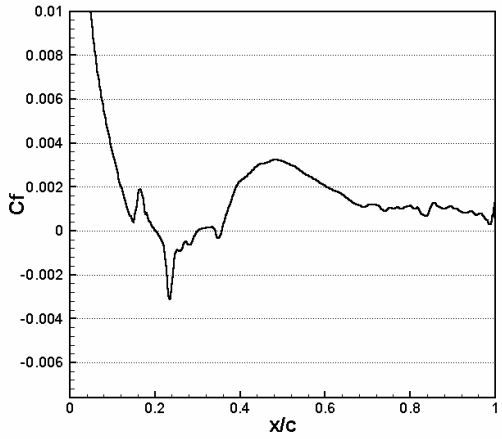

Figure 4.2.6 Skin friction coefficient distribution on the suction side

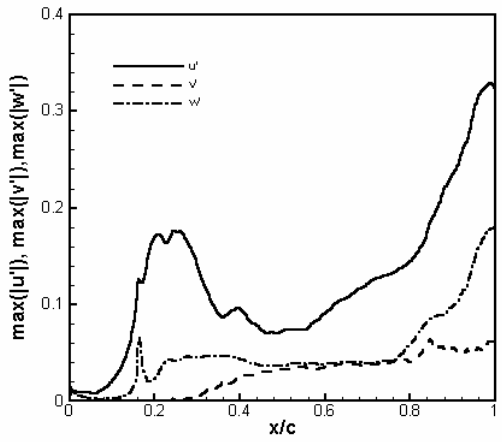

Figure 4.2.7 Peak r.m.s across the boundary layer

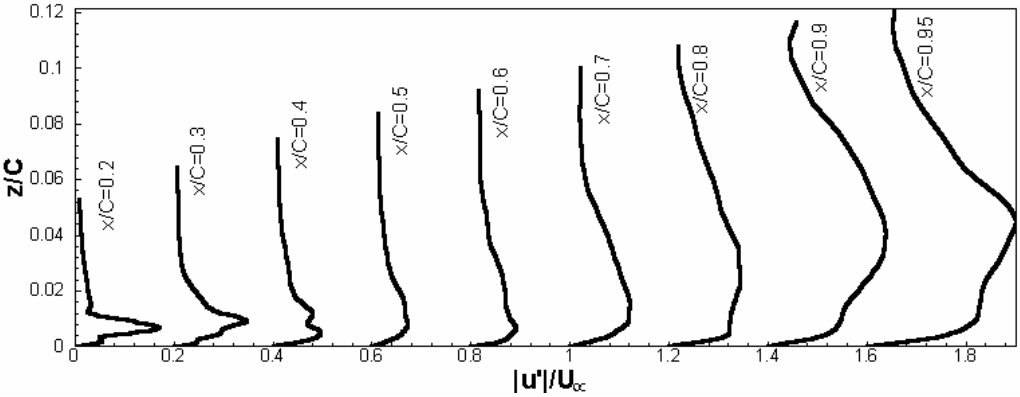

Figure 4.2.8 r.m.s streamwise fluctuation velocity profiles

The instantaneous vorticity in spanwise directions at different time are plotted in Figure 4.2.9. The simulation is started from the 2D solution as the baseline case. At the early stage of the simulation, we can see large vortex shedding. The unsteady blowing enforced before the separation point triggers the early transition of the boundary layer. The boundary layer reattaches shortly after separation and only forms a short separation zone. The reattached boundary layer further becomes fully turbulent. By comparing Figure 4.1.9 and Figure 4.2.8, the separated shear layer can be clearly seen in Figure 4.1.9. In Figure 4.2.9, the boundary layer is disturbed by the blowing and the transition takes place much earlier than in the non-blowing (baseline) case and the separation zone is significantly reduced.

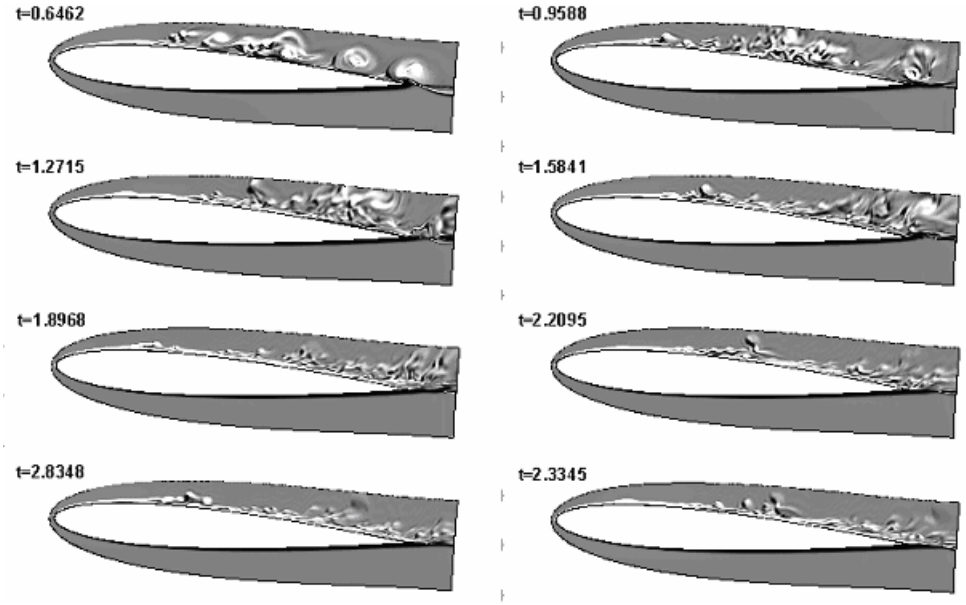

Figure 4.2.9 Instanteneous spanwise vorticity at different time

The iso-surfaces of vorticity components are plotted in Figure 4.2.10. The breakdown of the separated shear layer and the development of the vortex structure can be clearly seen. Instantaneous extrema of vorticity components are depicted in Figure 4.2.10. Compared to Figure 4.1.11, in this blowing case, large oscillations of the vorticity components appear much earlier than in the base line case, which indicates the early transition.

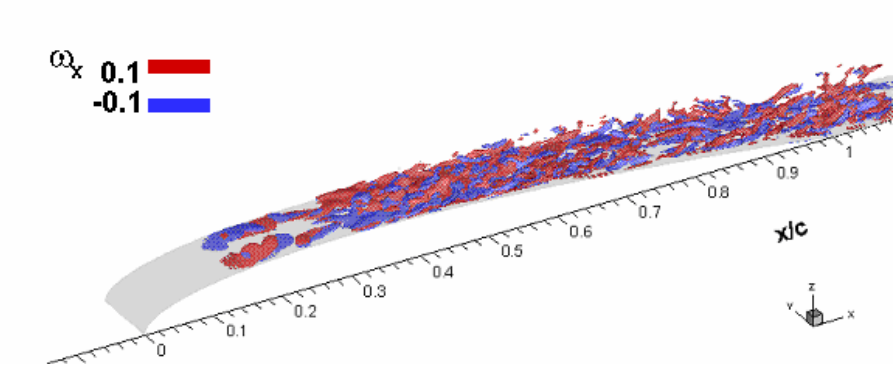

(a) streamwise vorticity

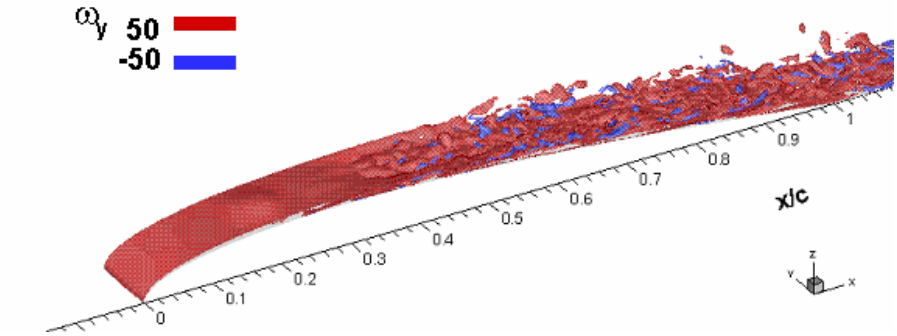

(b) spanwise vorticity

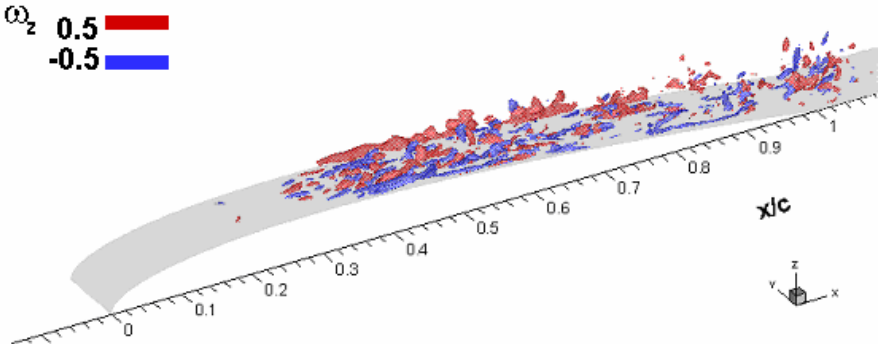

(c) wall-normal vorticity

Figure 4.2.10 Iso-surfaces of vorticity components

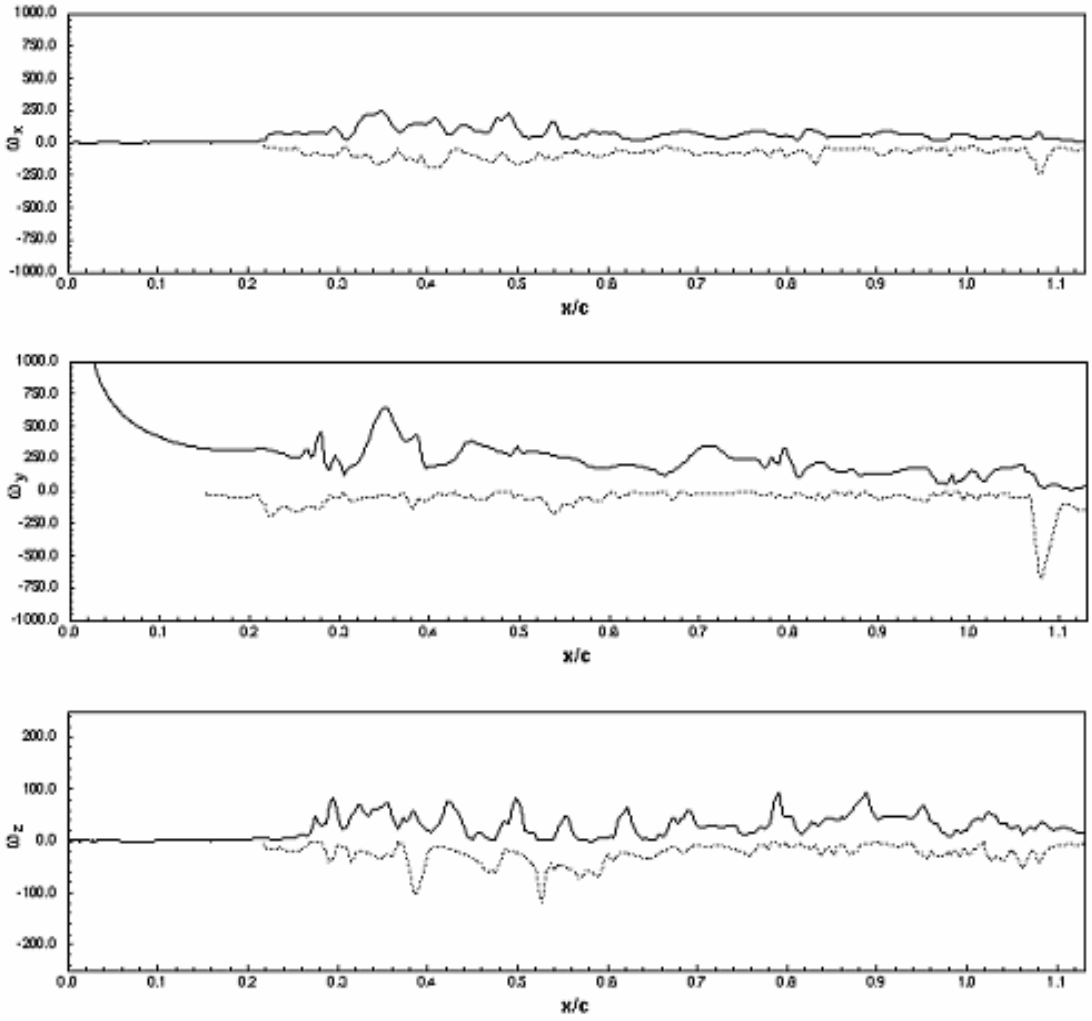

Figure 4.2.11 Instantaneous extrema of vorticity components

Figure 4.2.12 shows the spectrum of the streamwise velocity. Strong peaks at the pulsing frequency $\left(F^{+}=2\right)$ and harmonic multiples can be clearly seen at all locations, which means that the spectrum is dominated by the forcing frequency and its harmonics. Comparing with spectrum in baseline case (Figure 4.1.12), high frequency peaks appear earlier than in baseline case, indicating the early transition.

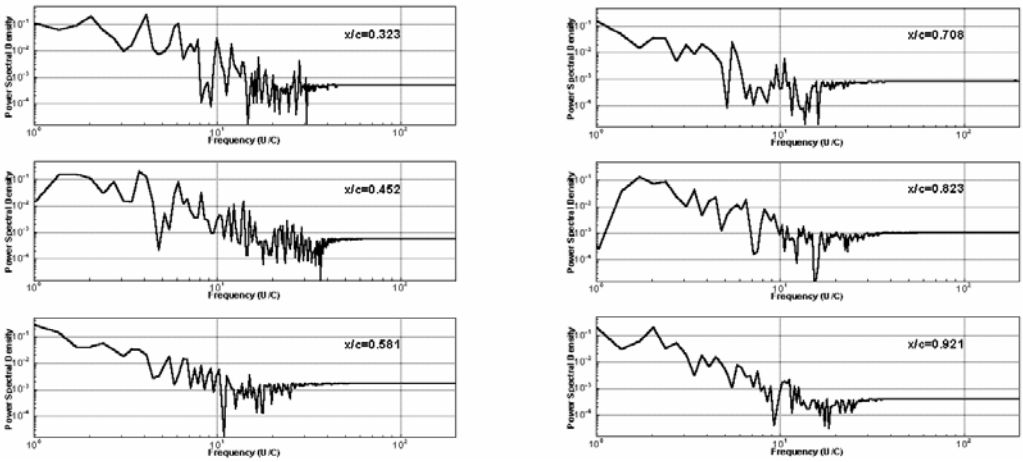

Figure 4.2.12 Power Spectral Density of streamwise velocity

From the simulation results and analysis of this pulsed blowing case, we conclude that properly selected unsteady blowing can trigger the early transition through exciting most unstable waves and non-linear interactions. In this case, we didn't observe the unstable mode picking up mechanism, because transition takes place in very short distance. This may be due to the large blowing mass flow which introduces a very large disturbance and leads to a bypass transition. To discover the unstable mode pick up mechanism, future selection of blowing jets should be with small blowing mass flow (very sharp shape in time with large k) and with a near vortex shedding frequency. Though the separation zone is reduced, both lift and drag are decreased. This shows that the increase of the ratio of lift over drag can happen for large attack angle, but not for small attack angles (4° for example in our case) although the separation is almost completely removed. Large attack angles for low Reynolds number flow may be selected as a target for future study of flow separation control where the ratio of lift over drag should be significantly improved.

4.3 The effect of blowing angle

To study the effect of blowing angle, we setup one case to simulate flow around the airfoil with pulsed blowing of 30^0 pitch angle and 90^0 screw angle. The pitch angle is defined as an angle between the blowing jet and wall surface. The screw angle is defined as an angle between the blowing jet and the inflow direction. This has been defined in section 4.2. The flow parameters and geometry are the same as the second case, except the blowing velocity has a pitch angle of 30^0. The vectors of blowing velocity are shown in Figure 4.3.1. The profile of the blowing velocity in streamwise and spanwise directions are also shown in Figure 4.3.1. One injection hole is centered at $y/c = 0.05$. In section 4.3.2, we will show another case with different non-dimensional frequency F^+=1.5 and much less mass flow of the blowing jets with large k=300.

4.3.1 Pitch blowing with F^+=2 and k=12

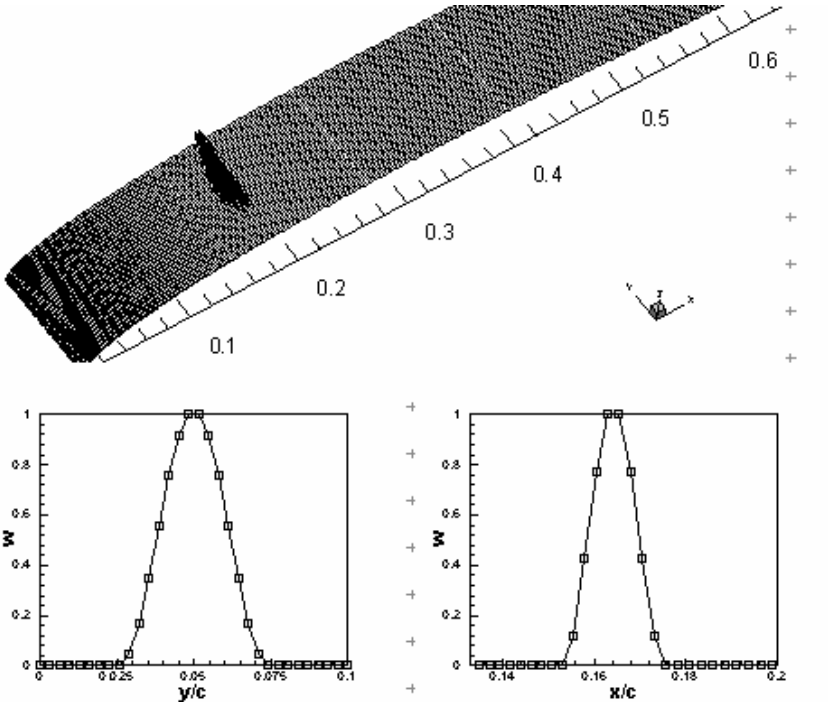

Figure 4.3.1 distribution of blowing velocity

This simulation was started from the solution of the baseline case at $t = 2.33C/U_\infty$. Time integration of this case has reached $t = 2.46C/U_\infty$. Time averaging is carried out over three periods of blowing. The reduced separation zone can also been seen from Figure 4.3.2 in which the maximum reverse velocity is depicted against streamwise location. Under the effect of blowing, the reversed flow appears in very short distance from $x/c = 0.2 \sim 0.4$. Compared with Figure 4.1.3, the reverse flow reaches the maximum value which is about 2% of free stream velocity. In the baseline case, the reverse flow velocity gradually increases and reach maximum of about 30% of the free stream velocity and the case of the pulsed blowing with no pitching is about 7%. Figure 4.3.3 shows the mean streamwise velocity profiles. We can find that the reversed flow completely disappears after $x/c = 0.4$, and the boundary layer becomes reattached to the surface afterwards.

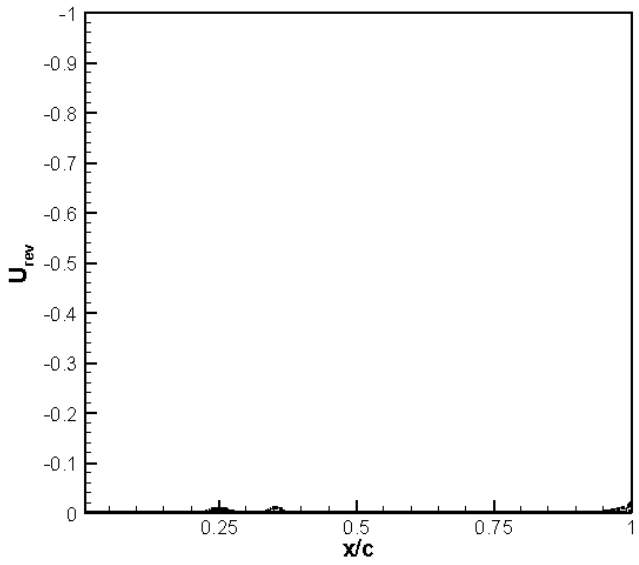

Figure 4.3.2 Mean reverse flow distribution on the suction side, $U_{rev} = \min(\overline{u})$

Figure 4.3.4 shows the r.m.s streamwise fluctuation velocity profiles at different x-locations. Inside the separation zone, from $x/c = 0.2 \sim 0.4$, the peak values can be seen inside the boundary layer, indicating the development of the instability waves. After reattachment, this multi-peak profiles no longer exist.

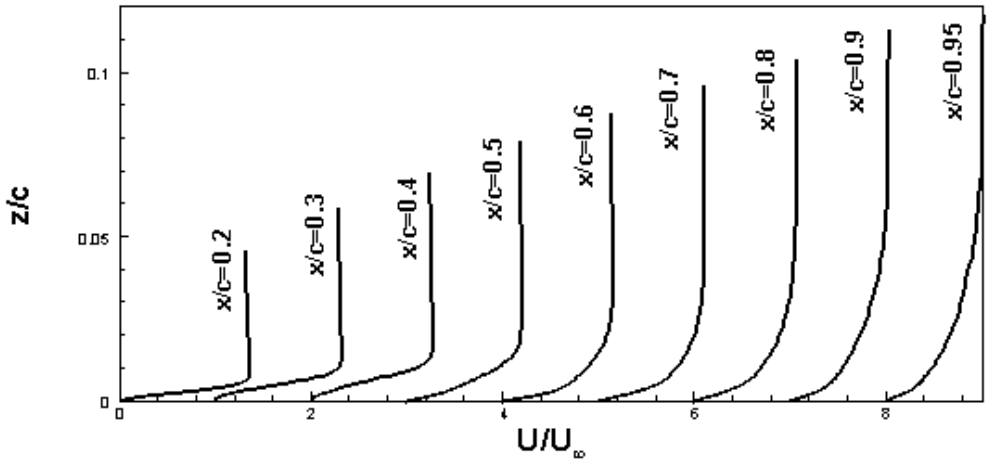

Figure 4.3.3 Streamwise mean velocity profiles

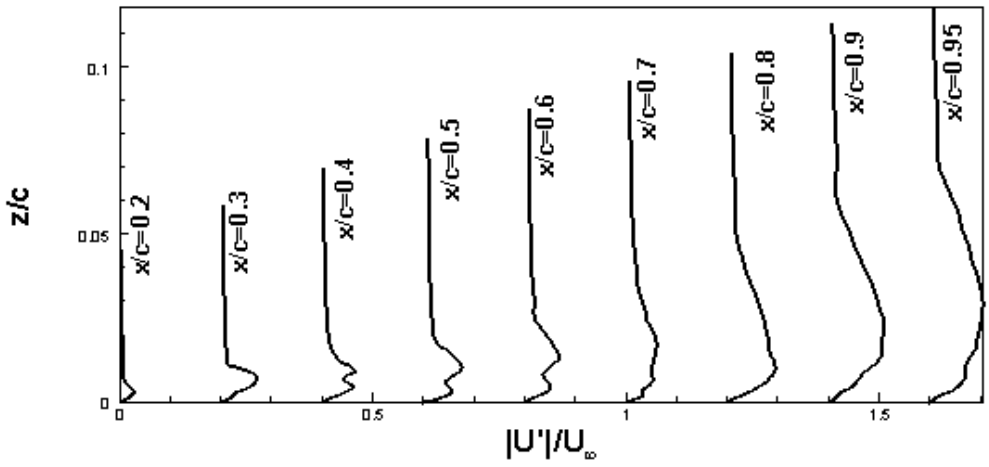

Figure 4.3.4 r.m.s streamwise fluctuation velocity profiles

The skin friction coefficient distribution on the suction side is shown in Figure 4.3.5. Figure 4.3.6 shows the peak r.m.s of the velocity fluctuations. In the separation zone, the skin friction coefficient is negative. Compared to the previous case with no skew angle, the separation region is about the same, but the friction coefficient in the separation region is now much smaller in absolute value and very close to zero. This indicates that the separation is better controlled with pitch and skew angle pulse. Around $x/c = 0.4$, there is a rapid growth of the skin friction, indicating the transition to turbulence occurs. The rapid growth of the streamwise and wall normal velocity fluctuations starts after the blowing injection point. After a very short distance, they reach a steady level. The growth rate of the spanwise velocity is more rapid than that in the baseline case. In this case, the transition takes place in very short distance and disturbance level is much lower than in the baseline case.

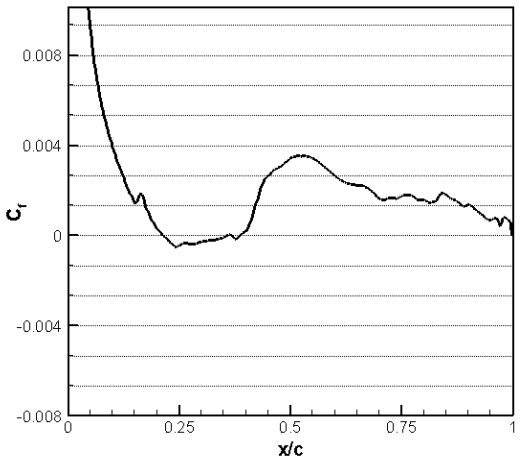

Figure 4.3.5 Skin friction coefficient distribution on the suction side

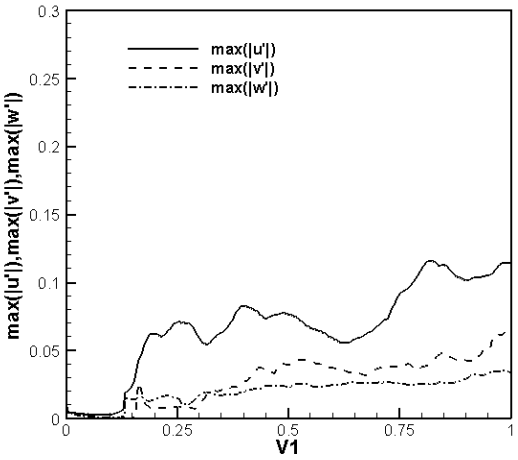

Figure 4.3.6 Peak r.m.s across the boundary layer

Temporal variations of lift and drag coefficients which are averaged over spanwise direction are shown in Figure 4.3.7. For the case with normal pulse, we observed the reduction of the separation zone reduces both drag and lift forces. While the case with skew angle pulse gives quite a better result. The lift force is maintained in high level and, at the same time, the drag force is reduced.

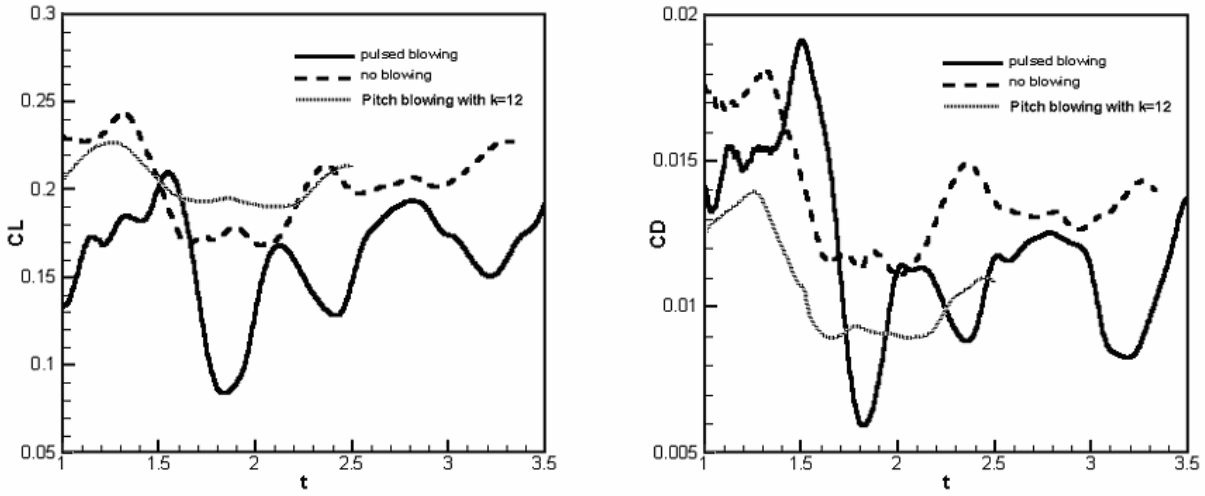

Figure 4.3.7 Temporal variations of lift and drag coefficients

Figure 4.3.8 shows the evolution of instantaneous spanwise vorticity. At the initial stage, the separation zone can be clearly identified. When disturbances introduced by the blowing jets enter the separated shear layer, disturbances are amplified when traveling downstream. At $t = 0.6253C/U_\infty$, we can see the rippling of the shear layer and the vortex shedding after the rippling. But in the later stages, the separation zone totally disappeared.

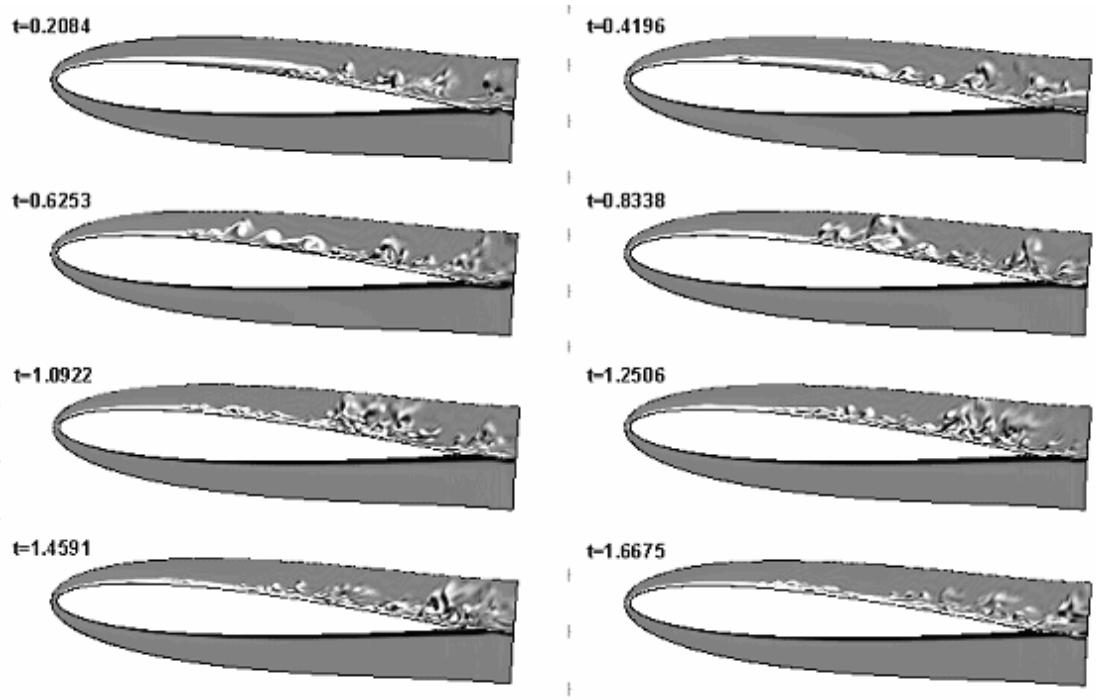

Figure 4.3.8 Instantaneous spanwise vorticity at different time

Figure 4.3.9 shows the iso-surface of instantaneous vorticity components at $t = 1.776C/U_\infty$. The experiment (Bons et al, 2001) shows the pitched jet will obtain a better efficiency due to the un-symmetric vortex structure. The same conclusion is found in our simulation as described above.

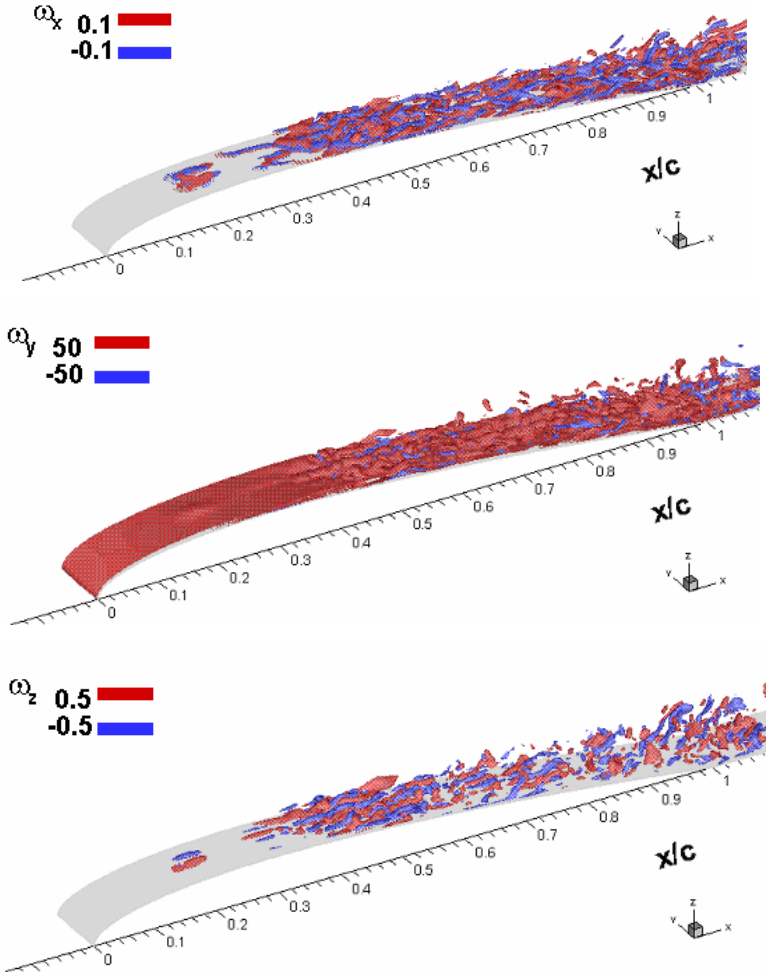

Figure 4.3.9 Iso-surface of vorticity components

4.3.2 Pitch blowing with F^+=1.5 and k=300

Shape functions in space and time which are used to define spatial distribution and temporal variation of the blowing velocity are depicted in Figure 4.3.10. To make it clear, Figure 4.3.11 shows an enlarged portion. $k = 300$ is used in this case. In this case, the blowing mass is around one fifth of the previous case in section 4.3.1. This simulation was started from the solution of the baseline case at $t = 2.33C/U_\infty$. Time integration of this case has reached $t = 1.78C/U_\infty$, which is insufficient and we need more time to run for this case. Time averaging is carried out over two periods of blowing.

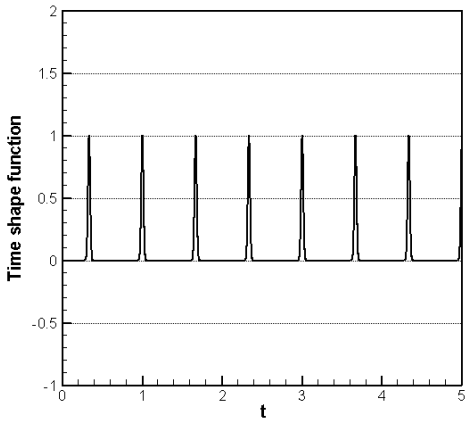

Figure 4.3.10 Shape functions in time

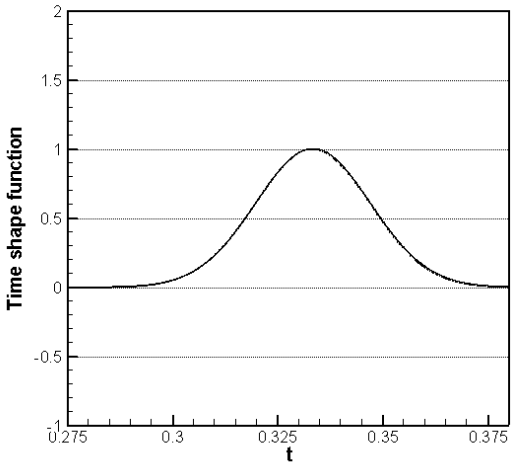

Figure 4.3.11 Shape functions in time

The reduced separation zone can also been seen from Figure 4.3.12 in which the maximum reverse velocity is depicted against streamwise location. Under the effect of blowing, the reversed flow appears in very short distance from $x/c = 0.2 \sim 0.4$, and the reverse flow reaches the maximum value which is about 2% of the free stream velocity.

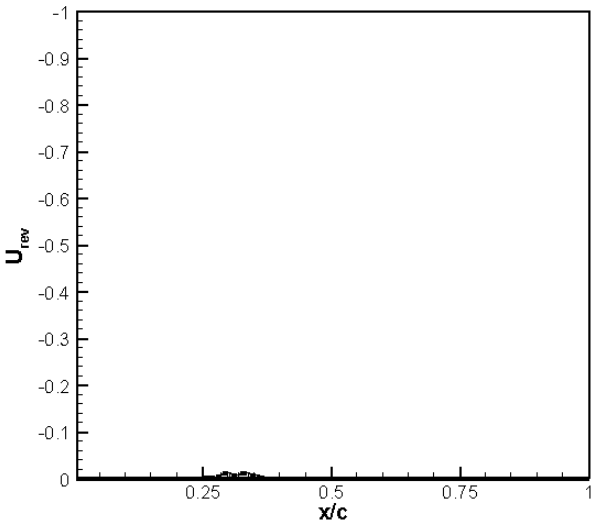

Figure 4.3.12 Mean reverse flow distribution on the suction side, $U_{rev} = \min(\overline{u})$

The skin friction coefficient distribution comparison on the suction side is shown in Figure 4.3.13. Figure 4.3.14 shows the peak r.m.s of the velocity fluctuations. Similar to previous cases, around $x/c = 0.4$, there is a rapid growth of the skin friction, indicating the transition to turbulence occurs. Compared to the previous case with a large blowing mass, the transition in current case happens earlier with much less blowing mass.

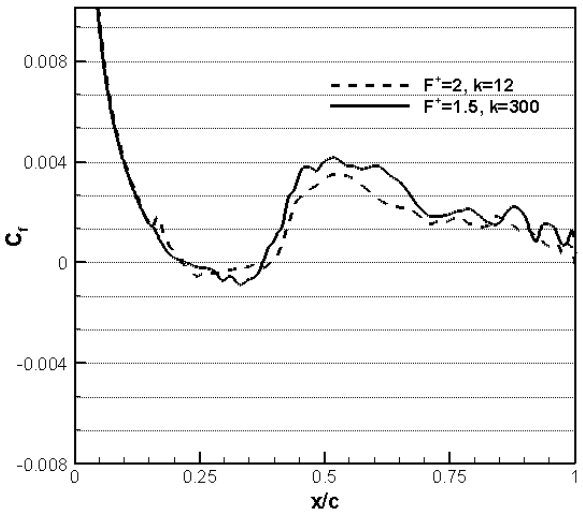

Figure 4.3.13 Comparison of skin friction coefficient distribution on the suction side

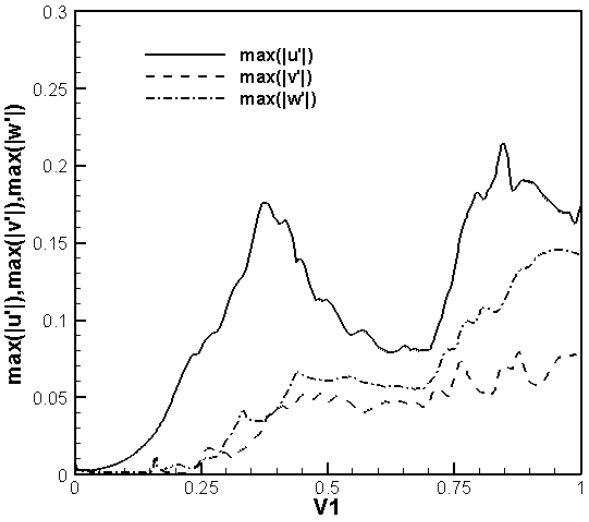

Figure 4.3.14 Peak r.m.s across the boundary layer

5. CONCLUSION

Separation and transition processes on a NACA 0012 airfoil with or without jet blowing on the surface have been investigated. The following conclusions are made based on our observations and results analysis.

1. The transition to turbulence on a 2D airfoil will reattach the separated boundary layer. Though no external disturbances are introduced, the initial perturbations may come from the up-ward traveling acoustic waves which are generated in the wake. The wake, which is a free shear layer with invicid instability, is most unstable and becomes unstable first. The separation points and the stagnation point are closely related to the pressure distribution on the airfoil surface. The upward traveling acoustic waves may affect the pressure distribution which further changes the location of separation points and stagnation points. This oscillation introduces perturbations inside the boundary. The perturbations are convected downstream as vortical disturbances. The separated shear layer has an inviscid instability and the perturbation will be quickly amplified in a rate much higher than the viscous instability. The traveling disturbances trigger instability waves which is identified as Kelvin-Helmholtz instability. The appearance of 3D motions of the shed prime vortex , where the stremwise vortex appears, and nonlinear interactions of disturbances lead to the sudden growth of disturbances and the generation of high frequencies. The breakdown then happens due to the interaction of spanwise and streamwise vortices. The shear layer becomes turbulent and reattaches to the surface. This process are then further sustained by the global feed back mechanisms

2. Properly selected unsteady blowing can trigger the early transition through exciting most unstable waves and non-linear interactions. In our cases, we didn't observe the unstable mode picking up mechanism, because transition takes place in very short distance. This may be caused by the large mass flow of the blowing jets which cause the bypass transition. Though the separation zone is reduced, both lift and drag are decreased.

3. With 30^0 pitch angle and 90^0 screw angle, the separation zone is reduced, drag are decreased while the lift maintain approximately the same level as in the base case, which show the pitch and screw angles are important to affect the efficiency of separation control by blowing jets.

4. By selecting appropriate blowing frequencies corresponding to the vortex shedding frequency $F^+ = 1.5$ and reducing the blowing mass (section 4.3.2), we also observed a similar reduction of the separation zone but an earlier transition than the previous case which has $F^+ = 2$ and much larger blowing mass (section 4.3.1).

Future work should focus the optimization of blowing jets by selecting the large attack angle, small mass flow with large k, and appropriate blowing frequencies corresponding to vortex shedding frequency which is around $F^+ = 1.4$ in our case.

The DNS data have been post-processed as a movie which can be obtained by sending a request to Dr. Chaoqun Liu at cliu@uta.edu.

ACKNOWLEDGMENT

This work was sponsored by the Air Force Office of Scientific Research (AFOSR) and monitored by Dr. Len Sakell and picked up by Dr. Tom Beutner later under grant number F49620-01-1-0028. The views and conclusions contained here should not be interpreted as necessarily representing the official policies or endorsements of the AFOSR or the US Government.

The authors also thank the High Performance Computing Center of US Department of Defense for providing supercomputer hours.

REFERENCE

[1] Bertolotti, F. P., Herbert, T., Spallart, P. R., “Linear and nonlinear stability of the Blasius boundary layer”, *Journal of Fluid Mechanics*, Vol. 242, pp441-474, 1992.

[2] Boiko, A. V., Grek, G. R., Dovgal, A. V., Kozlov, V. V., “The origin of turbulence in near-wall flows”, pp 167-196, *Springer*, 2002.

[3] Bons, J. P., Sondergarrd, R., and Rivir, R. B., 2001, “Turbine Separation Control Using Pulsed Vortex Generator Jets”, *Journal of Turbomachinery*, Vol.123, pp.198-206

[4] Drazin, P. G., Reid, W. H., “Hydrodynamic Stability”, pp1-50, *Cambridge University Press*, 1981.

[5] Lele, S. K., 1992, “Compact finite difference schemes with spectral-like resolution”, *Journal of Computational Physics*, Vol.103, pp.16-42.

[6] Jiang, L. Shan, H., and Liu, C. 1999. Direct numerical simulation of boundary-layer receptivity for subsonic flow around airfoil. *Recent Advances in DNS and LES*, *Proceedings of the Second AFOSR (Air Force Office of Scientific Research) International Conference*. Rutgers, New Jersey, June 7-9.

[7] Jiang, L. Shan, H., and Liu, C. 1999. Non-reflecting boundary conditions for DNS in curvilinear coordinates. *Recent Advances in DNS and LES*, *Proceedings of the Second AFOSR (Air Force Office of Scientific Research) International Conference*. Rutgers, New Jersey, June 7-9.

[8] Masad, J. A., Iyer, V., "Transition prediction and control in subsonic flow over a hump", *Phys. Fluids*, 6 (1), pp313-327, 1994

[9] Nagib, H., Kiedaisch, J., Greenblatt, D., Wygnanski, I., Hassan, A., 2001, "Effective Flow Control for Rotorcraft Applications at Flight Mach Numbers" , *AIAA Paper* 2001-2974, June, 2001.

[10] Shan, H., Jiang, L., and Liu, C. 2001. Numerical simulation of complex flow around a 85 delta wing. *Proceedings of the Third AFOSR (Air Force Office of Scientific Office) International Conference on DNS/LES*. Arlington, Texas, August 5-9.

[11] Shan, H., Jiang, L., and Liu, C. 2000. "Direct numerical simulation of three-dimensional flow around a delta wing". AIAA Paper 2000-0402, the 38th AIAA Aerospace Sciences Meeting and Exhibit, January 10-13, 2000, Reno NV.

[12] Yang, Z.Y., Voke, P.R., 2001, "Large-eddy simulation of boundary-layer separation and transition at a change of surface curvature", *Journal of Fluid Mechanics.* Vol.439, pp.305-333.

[13] Yoon, S., Kwak D., 1992, "Implicit Navier-Stokes solver for three-dimensional compressible flows", *AIAA Journal*, Vol.30, pp.2653-2659.

AVT-111 Specialists' Meeting on Enhancement of NATO Military Flight Vehicle Performance by Management of Interacting Boundary Layer Transition and Separation

DISCUSSION

1. REFERENCE No. OF THE PAPER: 5
2. DISCUSSOR´S NAME: S. Wagner
3. AUTHOR´S NAME: Liu, Jiang

QUESTION:

In some numerical computations we included some additional artificial disturbances in order to investigate the influence of disturbances that are always present in tunnel flow.

AUTHOR´S REPLY:

Our case (separation and transition around airfoil with attack angle) is self-excited and is not very sensitive to the inflow perturbation. Therefore, we did not put any artificial disturbances in the inflow to stimulate the real inflow.

1. REFERENCE No. OF THE PAPER: 5
2. DISCUSSOR´S NAME: H. Fasel
3. AUTHOR´S NAME: Liu, Jiang

COMMENT:

Results for secondary instability are wrong: Subharmonic (Herbert Breakdown) should depend on 2-D (!) amplitude and not on 3-D!! –

Code must leave too much diffusion ??!! This is a critical test for applicability of your code for transition simulations! (and since transition affects separation, code may not be applicable for these kind of separation control problems).

AUTHOR´S REPLY:

No reply.